Particle and Fibre Toxicology

RESEARCH

Open Access

Protective effect of Cordycepin on blood-testis barrier against pre-puberty polystyrene nanoplastics exposure in male rats

Ying Hu[1,2], Shuyi Jiang[1,3], Qiang Zhang[1], Wenjie Zhou[1], Jinhong Liang[1], Ying Xu[1*] and Wenhui Su[1*]

Abstract

Plastic pollution is an emerging environmental issue, with microplastics and nanoplastics raising health concerns due to bioaccumulation. This work explored the impact of polystyrene nanoparticle (PS-NPs) exposure during prepuberty on male reproductive function post maturation in rats. Rats were gavaged with PS-NPs (80 nm) at 0, 3, 6, 12 mg/kg/day from postnatal day 21 to 95. PS-NPs accumulated in the testes and reduced sperm quality, serum reproductive hormones, and testicular coefficients. HE staining showed impaired spermatogenesis. PS-NPs disrupted the blood-testis barrier (BTB) by decreasing junction proteins, inducing inflammation and apoptosis. Transcriptomics identified differentially expressed genes related to metabolism, lysosome, apoptosis, and TLR4 signaling. Molecular docking revealed Cordycepin could compete with polystyrene for binding to TLR4. Cordycepin alleviated oxidative stress and improved barrier function in PS-NPs treated Sertoli cells. In conclusion, prepubertal PS-NPs exposure induces long-term reproductive toxicity in male rats, likely by disrupting spermatogenesis through oxidative stress and BTB damage. Cordycepin could potentially antagonize this effect by targeting TLR4 and warrants further study as a protective agent. This study elucidates the mechanisms underlying reproductive toxicity of PS-NPs and explores therapeutic strategies.

Keywords BTB, Spermatogenesis, Polystyrene nanoplastics, Cordycepin

Introduction

Nowadays, plastics have already been ubiquitous in almost all terrestrial and aquatic ecosystems around the world. In the past few years, due to the epidemic of COVID-19, the use of a large number of disposable plastic protective equipment and packaging has worsened environmental plastic pollution. After entering into the environment, plastic materials of various chemical nature (polyethylene, polypropylene, polyvinyl chloride, polystyrene, polyethylene terephthalate, et al.) could be degraded into microplastic (MPs, 0.1 μm-5 mm) and nanoplastic (NPs, <0.1 μm) particles under the action of physical, chemical, biological and other factors [1–3], which have appeared in oceans, freshwaters, sediments and atmospheric fallout around the world [4]. Due to large amount

*Correspondence:
Ying Xu
yxu@cmu.edu.cn
Wenhui Su
whsu@cmu.edu.cn
[1]Department of Biochemistry and Molecular Biology, College of Life Science, China Medical University, No. 77 Puhe Road, Shenyang North New Area, Shenyang, Liaoning Province 110122, China
[2]National Clinical Research Center for Laboratory Medicine, Department of Laboratory Medicine, Units of Medical Laboratory, The First Hospital of China Medical University, Chinese Academy of Medical Sciences, Shenyang 110001, China
[3]Center of Reproductive Medicine, Shengjing Hospital of China Medical University, Shenyang, China

and poor biodegradability, the health impacts of MPs/NPs have become one of the frontier hotspots in the field of international environment in these years. In 2022, plastic particles (>700 nm) were discovered and quantified for the first time in human blood by a double shot pyrolysis-gas chromatography, suggesting plastic particles are bioavailable for human body [5]. Plastic particles invade the human body primarily through the alimentary tract [6], and also through the respiratory system [7, 8], cutaneous mucosal [9], and injection pathway [10]. Furthermore, sub-micron particles are theoretically more easier to traverse biological barriers and membranes and accumulate in organs, thereby causing pathological damage [11, 12]. Thus, it is necessary to investigate the potential biological effects of MPs/NPs and develop effective prevention measures.

As an important thermoplastic, polystyrene (PS) is one of the high-yield plastics with a wide range of applications, accounting for 90% of total plastic demand, especially in one-off packaging, containers, personal care products and electronics [13, 14]. PS-NPs is an organic nanocomposite material formed by polystyrene nanoparticles dispersed in a polymer matrix at the nanoscale size, which is easy to form aggregates in protein-containing media, produce combined toxicity with other organic matter, and enter cells and organelles to exert toxic effects [6, 15].

In recent decades, male fertility is declining due to dietary behavior, lifestyle and environmental chemistry [16, 17]. A growing number of researches have posed health concerns about the deleterious effects of environmental plastic particles on male reproduction, typically related with inflammatory responses, oxidative stress, genetic toxicity in reproductive cells and decreased fertility in individuals [18–21]. However, the studies on the reproductive toxicity of various plastic pollutants was mainly carried out in aquatic organisms and terricolous invertebrates [22–24]. Recently, a study on PS-NPs in mouse revealed its testicular and sperm toxicities, including damaged testicular microstructure, reduced sperm count and quality, and inhibited sperm capacitation, yet the mechanisms still remained to be clarified [25].

Blood-testis barrier (BTB) is the structure between spermatogenic tubules and capillary blood, composed of the capillary endothelium, the connective tissue, the basal membrane of seminiferous epithelium and cell junctions, such as tight junction (TJ), ectoplasmic specialization (ES, a testis-specific adherens junction), and desmosome-like junction, between Sertoli cells (SCs). BTB can prevent certain substances from entering the seminiferous epithelium, form and maintain an independent microenvironment conducive to spermatogenesis, and prevent spermatogenic substances from escaping outside the tubules and causing an autoimmune reaction [26]. Exposure to environmental toxicants has been show to lead to restructuring or disruption of the BTB and thus result in spermatogenesis dysfunction [27, 28]. Although PS-MPs has been proved to associate with SC microstructural damage, increased permeability of the BTB and incomplete spermatogenesis [29–33], the mechanism on molecular level still remains unknown and little attention has been paid to the influence of PS-NPs on the BTB function.

The prevailing data suggest that the MPs content in infant excrement was significantly greater than that in adult excrement [34], indicating that infant are more vulnerable than adults to MPs exposure. Furthermore, there is currently limited research on the mechanisms underlying testicular damage and abnormal spermatogenesis induced by exposure to PS-NPs in prepubertal mammals [35]. Therefore, the objective of our study was to investigate the reproductive damage effect and mechanisms of PS-NPs in pre-pubertal male rat and to screen the effective drug preliminarily based on the mechanism discovered. We treated prepubertal male rats with different doses of PS-NPs and detected the variation in sperm quality, BTB function, serum reproductive hormones, and testicular morphology to evaluate the detrimental effects of PS-NPs exposure during adolescence on male reproductive system after maturation. Based on the consequence of RNA-sequencing, a protein-protein interaction network using differentially expressed genes from PS-NPs-exposed rat testis transcriptomes was constructed to screen for key target proteins that interact with polystyrene. Then, utilizing molecular docking and molecular dynamics simulation, we identified the optimal anti-oxidative stress drug, i.e. Cordycepin, that could target the same sites of toll-like receptor 4 (TLR4) as polystyrene, and confirmed its antagonistic effect on PS-NPs in primary cultured SCs. These experiments provide experimental evidence for further elucidating the reproductive toxicity mechanisms of PS-NPs and offer potential intervention strategies to prevent reproductive damage caused by PS-NPs.

Materials and methods

Materials

Unibead Uniform Polystyrene Microspheres and Lumisphere Uniform Green Fluorescent Microspheres, both of which are about 80 nm in diameter and composed of polystyrene (PS), were procured from the Tianjin Baseline Chromtech Research Centre (Tianjin, China). Except for fluorescein isothiocyanate (FITC) labeling, the two particles have the same physicochemical properties. The PS-nanoparticles were analyzed to confirm the morphology, size, and chemical composition by scanning electron microscope (SU8020, Hitachi, Japan), Zetasizer (Nano ZS90, Malvern, UK), and Fourier transform infrared

spectroscopy (FTIR, Nicolet IS10, USA) respectively. These nanoparticles were suspended in purified, deionized water at a concentration of 2.5% w/v. In experiments to detect the distribution and accumulation of PS-NPs in tissue, the green fluorescence-labeled particles, with excitation and emission peaks at wavelengths of 488 nm and 518 nm respectively, were diluted to 1.0% w/v. Throughout the duration of the study, nanoplastic stock solutions were preserved under refrigeration at 4 °C, shielded from light exposure. Prior to utilization, the PS-NPs stocks were subjected to sonication on ice for 15 min at a frequency of 50/60 kHz.

Animals and treatment

48 male Sprague-Dawley (SD) rats in good health (body weight 60–80 g) were obtained from SPF (Beijing) Biotechnology Co., Ltd (Certification number: 110324211105179853). The temperature of the feeding environment is controlled at 20–22℃, and the humidity is controlled at about 60%, with a 12-hour cycle of light and darkness. The rodents were divided into four groups randomly and gavaged with varying doses of PS-NPs (0, 3, 6, and 12 mg/kg/day) according to previous reports [36, 37] via a 5 ml syringe at the pharynx to avoid particle loss from postnatal day (PND) 21. An equivalent volume of distilled water without nanoparticles was given to the control animals. The gavage volume was recalculated weekly based on changes in body weight to maintain consistent dosage. Animals had unrestricted access to purified water and were provided with a standardized pelleted maintenance feed, including the following constituents (per kilogram) according to the information provided by the supplier: glucose, 710 g; ovalbumin, 155 g; cellulose, 30 g; corn oil, 28 g; coconut fat, 17.75 g; vitamin premix, 12 g; mineral premix, 10 g; NaH_2PO_4-$2H_2O$, 14.5 g; $CaCO_3$, 12.4 g; $KHCO_3$, 7.7 g; $MgCO_3$, 1.4 g; KCl, 1.0 g and KIO_3, 0.25 mg. The Test Report of the maintenance feed provided by the supplier showed no micro- or nano- plastic interference. The sole source of water intake was a glass bottle capped with a steel stopper, which were assigned to each experimental group in order to avoid cross contamination. Water and food intake were also recorded weekly until the animals were terminated on PND55 or PND95 to evaluate the long-term effects of PS-NPs. After anesthetization by CO_2 inhalation, blood samples were collected via cardiac puncture, and serum was isolated immediately by centrifugation and preserved at -80 °C for future assays. The epididymides and testes were dissociated and weighed for organ coefficient calculations before preservation at -80℃ for subsequent experiments.

Observation of PS-NPs accumulation in rat testis

Rats were given 80 nm green fluorescent PS-NPs (3 mg/kg/day) or ddH_2O by oral gavage every day for one week from PND21 (n=5). The animals were terminated by CO_2 asphyxiation immediately after the last treatment. After removal of testis, fluorescence images of one testis tissue of the rat were observed under fluorescent stereomicroscope (M165 FC, LEICA, Germany). Frozen Sect. (100 μm) from the other testis of the rat were prepared by a vibratome (VT1200S, LEICA, Germany) and visualized via laser scanning confocal microscope (LSM 980, Carl Zeiss, Germany).

Reproductive hormone detection

Testosterone (T), luteinizing hormone (LH), and follicle-stimulating hormone (FSH) in collected serum samples were detected by commercial kits (ZellBio GmbH, Germany) and quantified through enzyme-linked immunosorbent assay (ELISA) as per the manufacturer's specification. Each ELISA test included three technical replicates to ensure accuracy and reproducibility.

Sperm evaluation

Sperm quality was assessed after rapid dissection of the rat epididymis. For sperm motility analysis, the caudal part was separated, ground and incubated in phosphate buffered saline (PBS, pH7.5) at a temperature of 37 °C to allow releasing of viable sperms. After 15 min, sperms in the supernatant and the suspension were respectively tallied with a hemocytometer, the ratio between which was used to represent sperm motility. For morphological examination, fresh spermatozoa were gathered by slitting open equivalently sized caudal epididymides, which were immersed in PBS at 37 °C and gently pipetted to coax sperm out of the tubules. Afterwards, a droplet of the sperm suspension was smeared onto a sterile adhesive glass slide, spread across, and air-dried before observation. A total of 300 sperms from each specimen were scrutinized for morphological defects under magnification, with the anomaly percentage computed by the fraction of malformed sperm over the entire sperm count. For each rat, five smear slides were prepared, and within those, 12 random high-power fields were examined to tally the sperm counts.

Hematoxylin & eosin staining

Rat testes were promptly immersion-fixed in Bouin's fixative at a ratio of 10:1 of fixative to testicular tissue volume following removal. The fixed testis was trimmed and then rinsed with running tap water for 4 h. Subsequently, dehydration was performed by gradually increasing the concentration of ethanol, starting from lower concentrations to higher ones (i.e., 70% for 2 h, 80% overnight, 90% for 2 h, 100% I for 1 h, and 100% II for 1 h). The tissue

was then cleared in xylene for 30 min until the specimen became transparent. The tissue blocks were transferred into a xylene-paraffin mixture and were permeated with wax at 60 °C for 2 h before paraffin embedding. The tissues were then cross-sectioned into 5 μm-thickness slice using a microtome and mounted on glass slides. For histological analysis, paraffin wax sections were deparaffinized in xylene and rehydrated in ethanol solution with decreasing concentration and water in sequence. Sections were then incubated with hematoxylin for 4 min, washed with tap water, differentiated in hydrochloric acid alcohol, and counterstained with eosin for 60 s. After dehydration in ethanol with increasing concentration and xylene, sections were mounted in neutral balsam and dried for observation. Images were detected and captured by a microscope outfitted with a high-resolution digital camera.

Immunohistochemistry

Antigen retrieval was performed after deparaffinization and rehydration of the testis sections, followed by washing with PBS. Then the slices were blocked with 10% goat serum before incubation with anti-Bcl-2 (1:100) or Bax (1:300) antibodies (Tab.S1) and maintained at -4 °C throughout the night. Subsequently, the slices underwent a 60-min incubation at ambient temperature with a horseradish peroxidase (HRP)-conjugated secondary antibody. Following this, the slices were developed with diaminobenzidine (Gene Tech, Shanghai, China), counterstained using hematoxylin, and subjected to a sequence of dehydration, clarification, and mounting before observation under a light microscope (Echo, USA). Immunohistochemistry images were analyzed using Image-Pro Plus software (Media Cybernetics, Inc.). The images were imported, and the settings were adjusted to enhance the visibility of the stained areas. Use the "Thresholding" tool to define the regions of interest (ROI) where the staining is present. Select the "Measure" function and choose the appropriate parameters to calculate the optical density within the ROI. Record the Average Optical Density (AOD) values for each ROI. Export the data for further analysis or reporting. For each tissue slice, twelve representative microscopic fields were chosen at random.

BTB integrity assay

The BTB integrity was assessed through an established in vivo method that measures the barrier's capacity to impede the passage of diminutive molecular indicators from the underlying basal lamina, as previously detailed in the literature [38]. To serve as positive controls for disrupted BTB function, rats received an intraperitoneal injection of cadmium chloride ($CdCl_2$, 5 mg/kg) 72 h prior to the assay, based on its documented effect to destroy the BTB irreversibly. Before termination, the animals were sedated with an intramuscular injection of ketamine HCl combined with xylazine and an incision shorter than 10 mm was made on the scrotum to expose the testis. Then 50 μl of Sulfo-NHS-LC-Biotin (10 mg/ml, Thermo Fisher Scientific, USA) freshly diluted in PBS containing $CaCl_2$ (1 mM) was injected into the interstitium of testis to serve as the molecular tracer. Allowing for a 30-minute period for the biotin to disperse, the rats were then euthanized by CO_2 inhalation. Subsequently, the testes were extracted and quickly frozen in liquid nitrogen, followed by Sect. (10 μm) preparation at -20 °C using a cryostat and fixation with 4% paraformaldehyde. After blocking with 5% BSA, the sections were incubated with streptavidin labelled by Alexa Fluor 568, diluted at 1:200 in PBS with 1% BSA, and kept at ambient temperature for one hour. And then an Antifade Mounting Medium with DAPI (Beyotime, China) was used for mounting before the BTB damage was evaluated by fluorescence microscopy (BX60, Olympus, Japan). To quantitatively analyze the impairment of the BTB, we calculated the ratio of the distance that the biotin traveled (D_{biotin}) to the radius of the tubule (D_{radius}), denoted as [D_{biotin}/D_{radius}] × 100%. Utilizing Image J (1.52t) software, the migration distance of biotin was measured from the basal lamina of the tubule to the utmost extent of biotin penetration into the lumen. In each experimental cohort, 100 tubules from a total of 6 rats were randomly examined to ensure statistically significant results.

Transmission electron microscopy analysis

Sample tissues from testes were fixed with glutaraldehyde (2.5%) and osmium (1%) for ultrastructural analysis via electron microscopy before dehydration in ethanol. After washing with acetone, the samples were embedded within the epoxy resin matrix [39]. The embedded specimens were then sectioned into ultra-thin slices ranging from 50 to 60 nanometers in thickness with a precision ultramicrotome (UC7, Leica, Germany). These sections were then subjected to staining using a combination of uranyl acetate and 2% lead citrate to enhance contrast. High-resolution imaging of these prepared sections was performed using a 120 kV transmission electron microscope (HT-7800, Hitachi, Japan), which features a sophisticated Complementary Metal-Oxide Semiconductor (CMOS) detection camera (Hitachi, Japan).

Real-time reverse transcriptase polymerase chain reaction (qRT-PCR)

TRIzol (Invitrogen, USA) was used for extraction of total RNA from rat testis, the purity and concentration of which was determined by a spectrophotometer (BioDrop, UK). Afterwards, mRNA was reverse transcribed into cDNA by SuperScript III reverse transcriptase

(Invitrogen, USA). PCR amplification was conducted in 25 µl volume using the Takara SYBR Green protocol, involving an initial 3-min denaturation at 95 °C, then 40 cycles of denaturation at 95 °C for 10 s, annealing at 58 °C for 30 s, and elongation at 72 °C for 1 min. Specificity checks included melt curve assessments. The sequence of PCR primers is shown in Supplementary Table S2 [40, 41]. To normalize gene expression data, GAPDH served as the internal reference control. The comparative expression of the investigated mRNAs was quantified using the $2^{-\Delta\Delta Ct}$ approach.

Terminal deoxynucleotidyl transferase-mediated nick end labeling (TUNEL) staining

To ascertain apoptotic occurrences within the rat testis of rats, TUNEL assay (MK1027, Boster Biological Technology, China) was performed using paraffin-embedded testis sections, following the protocol provided by the kit's manufacturer. After the staining and mounting with an anti-fading reagent, and the sections were examined under a fluorescence microscope (BX60, Olympus, Japan). Nuclei that exhibited green fluorescence were identified as apoptotic. For each tissue section, ten different microscopic fields were chosen at random and intensity of the fluorescence was measured and quantified with the aid of Image J (v. 1.52v).

Transcriptome profiling and protein-protein interaction analysis

RNA-sequencing of three testis samples randomly chosen from the control and the 12 mg/kg/day group on PND95 was performed on BGISEQ-500 (BGI Genomics, China). Criteria for differentially expressed genes (DEGs) identification included a Q-value below 0.01 and a fold change magnitude exceeding 1.5. R Studio with ggplot2 package and internet-based platforms (https://www.omicstudio.cn/tool and http://www.bioinformatics.com.cn) were utilized for bioinformatics analyzing. Utilizing the OmicStudio resource (https://www.omicstudio.cn/tool) according to the GSEA 3.10 protocol, gene set enrichment analysis (GSEA) probed further into gene expression patterns and associated biological themes. Gene sets with significant enrichment were defined by a *P*-value threshold of less than 0.05. The RNA-sequencing data have been deposited on the NCBI (http://www.ncbi.nlm.nih.gov/) database as individual BioProjects under the umbrella BioProject PRJNA1124596. The data of styrene target were retrieved using SEA database (https://sea.bkslab.org/). Analysis of the data, alongside mapping of Protein-Protein Interaction Networks (PPI), was carried out via the Dr. Tom platform by BGI Tech (https://www.bgi.com/global/dr-tom/).

Molecular docking

The structures of antioxidant stress drugs were procured from the PubChem database (https://pubchem.ncbi.nlm.nih.gov) and optimized by LigPrep. The 3-dimentional structures of protein were retrieved from RCSB database. Molecular docking of proteins and drugs was performed using Maestro version 11.5. Moreover, energy minimization of proteins was accomplished at a protonation state of pH 7±2.0 via the OPLS-2005 force field. To test docking parameters, grid-based ligand was utilized to dock in the protein's catalytic pocket in the mode of Energetics of "extra precision" (Glide V11.5, Schrödinger). Lastly, the docking results were visualized using PyMOL2.3.0 software and Discovery Studio 2020 in composite PDB format.

Molecular dynamics simulations

Amber 22 (San Francisco, CA, USA) was applied to perform Molecular dynamics simulations [42]. The preprocessing of small molecules involved the employment of AmberTools22 for the integration of the GAFF force field into the molecular structures. Concurrently, the software Gaussian 16 W facilitated the hydrogenation of the small molecules and the computation of RESP charges; this information was subsequently incorporated into the topological data of the molecular dynamics framework. The simulations proceeded under conditions of fixed temperature (300 K) and pressure (1 atmosphere), using the ff19SB force field to compute system force field parameters [43]. Upon completion of simulations, calculations of the Root Mean Square Deviation (RMSD), Root Mean Square Fluctuation (RMSF), radius of gyration (Rg), solvent accessible surface area analysis (SASA), hydrogen bond analysis, along with associative free energy analysis using MMPBSA.py, were performed based on the trajectories of each amino acid.

Primary culturing of Sertoli cells and barrier function analysis in vitro

Utilizing previously established methods [44, 45], SCs were isolated from the testes of 20-day-old rats. These primarily isolated SCs were seeded onto culture dishes coated with Matrigel (BD BioSciences, USA) at varying densities tailored for distinct experimental analyses: immunoblotting at 0.3×10^6 cells/cm^2, barrier function tests at 1.0×10^6 cells/cm^2 on Millicell-HA inserts (Millipore, USA), and immunofluorescence at 0.03×10^6 cells/cm^2 on glass cover glass. The SCs were cultivated at 35 °C with 5% CO_2 environment in a serum-free medium (DMEM/F12, Gibco, USA) replenished with bacitracin (5 µg/ml), epidermal growth factor (2.5 ng/ml), insulin (10 µg/ml), and transferrin (5 µg/ml). The culture medium was refreshed daily over a 7-day period. To enhance SCs purity beyond 98%, on the second day,

cells underwent a brief hypotonic shock in Tris buffer (20 mM, pH 7.4) for 2.5 min at ambient temperature, effectively eliminating the residual germ cells. On day 3, SCs were administered with PS-NPs (5, 20, 100 μg/ml) for 24 h. In group (100 μg/ml) to confirm the recovery effect of Cordycepin, 20 μg/ml Cordycepin diluted in DMSO was added 30 min before PS-NPs treatment. The SC epithelial barrier function was detected by measuring the trans-epithelial resistance (TER) value and sodium fluorescein (Na-F) permeability each day from culture day 1 to day 7 as previously described [46]. In cell experiments, the Corning brand consumptive materials (pipette tips, culture plates, etc.) with good corrosion resistance and glass vials were identically applied to the control group and the treatment groups.

Oxidative stress assay

After treatment of PS-NPs and Cordycepin, the activity of CAT in SCs was analyzed with a CAT kit (Solarbio, Beijing, China). Using a Tecan Infinite M200 multifunctional enzyme reader, the absorbance of SC lysate supernatant at a wavelength of 240 nm was monitored. 2',7'-dichlorofluorescein diacetate (DCFH-DA) and JC-1 were applied to detect the reactive oxygen species (ROS) and assess the mitochondrial membrane potential, respectively. Specifically, SCs were incubated with either DCFH-DA or JC-1 in dark at 35 °C for 20 min after a double wash in PBS. Subsequently, cells were rinsed thrice using either PBS for DCFH-DA or the buffer specific for JC-1 detection. The resultant fluorescence was captured on the fluorescence microscope (BX60, Olympus, Japan). Quantitative analysis of the fluorescence intensities for each experimental cohort was executed with Image J (v. 1.52v).

Immunoblot analysis

For tissue samples, testes of each experimental cohort underwent triple washes in PBS. A precise mass of the testicular sample was cut, weighed, and subsequently submerged into a RIPA buffer solution fortified with phosphatase inhibitor, PMSF, and protease inhibitor. This preparation was then homogenized on ice and subjected to centrifugation (4,000 g) at 4 °C for 10 min. For cell samples, freshly cultured SCs were harvested and lysed by sonication on ice, followed by centrifugation (16,000 g) at 4 °C for 60 min. The resultant lucid supernatants were then secured and preserved at -80 °C. A BCA protein assay kit (Solarbio, China) was employed to quantify the total protein content in the testis or SC samples from one experiment, which were simultaneously prepared to preclude inter-experimental variations. For gel electrophoresis, a consistent quantity of protein (30 μg) from each set was thermally denatured at 100 °C for a span of 5 min, resolved on SDS-polyacrylamide gels with a concentration range from 4 to 15%, and then transferred onto PVDF membranes. These membranes underwent a sequential process of immunoblotting utilizing designated primary and secondary antibodies (refer to Tabl.S1). Post immunoblotting, membranes were rinsed with tris buffered saline (TBS) and target proteins were detected using an advanced chemiluminescence detection kit (Pierce Chemical, USA) with the ChemiDoc XRS system for image capture (Bio-Rad, USA). Further quantitative analysis of the image intensity was executed by Scion Image (4.0.3), with GAPDH serving as the internal standard.

Immunofluorescence analysis

To identify the precise distribution of BTB proteins, frozen testicular slices or SCs plated on glass slips underwent fixation with paraformaldehyde (4%), followed by permeabilization using Triton X-100 (1%) and subsequent blocking with bovine serum albumin (5%). These samples were then incubated with primary antibodies as listed in Table S1 at 4 °C throughout the night. After mounting with the Antifade Mounting Medium containing DAPI (Beyotime, China), the samples were examined with a fluorescence microscope (BX60, Olympus, Japan). A SpotRT digital camera was tasked with capturing the images, which were subsequently layered using Adobe Photoshop. All images shown herein are exemplary of consistent findings observed across six independent experiments.

Statistical analysis

Data of this research were statistically analyzed by SPSS 23.0 (SPSS Inc., USA). To assess differences, one-way ANOVA was performed, complemented by the Kolmogorov-Smirnov and Levene tests for comprehensive data evaluation. Results are shown as the mean±standard deviation (SD). A value of $P<0.05$ was deemed to denote statistical significance. The findings discussed are grounded on samples representative of each cohort, with an in vivo group size of six ($n=6$) or a minimum of three separate in vitro experiments involving SCs isolated from various rat cohorts.

Results

Testicular accumulation of 80 nm PS-NPs in rats after oral administration

Initially, the PS-NPs (80 nm) applied herein were identified and photographed via scanning electron microscopy (SEM). SEM images depicted a uniform spherical shape of the particles (Fig. 1A) and Raman spectroscopy demonstrated the polystyrene nature (Fig. 1B). Similarly, potential measurements confirmed that the PS-NPs used in our research were negatively charged on surface (-43.4 mV) (Fig. 1C), reflecting the low aggregation behavior of plastic nanoparticles. To ascertain the cumulation of

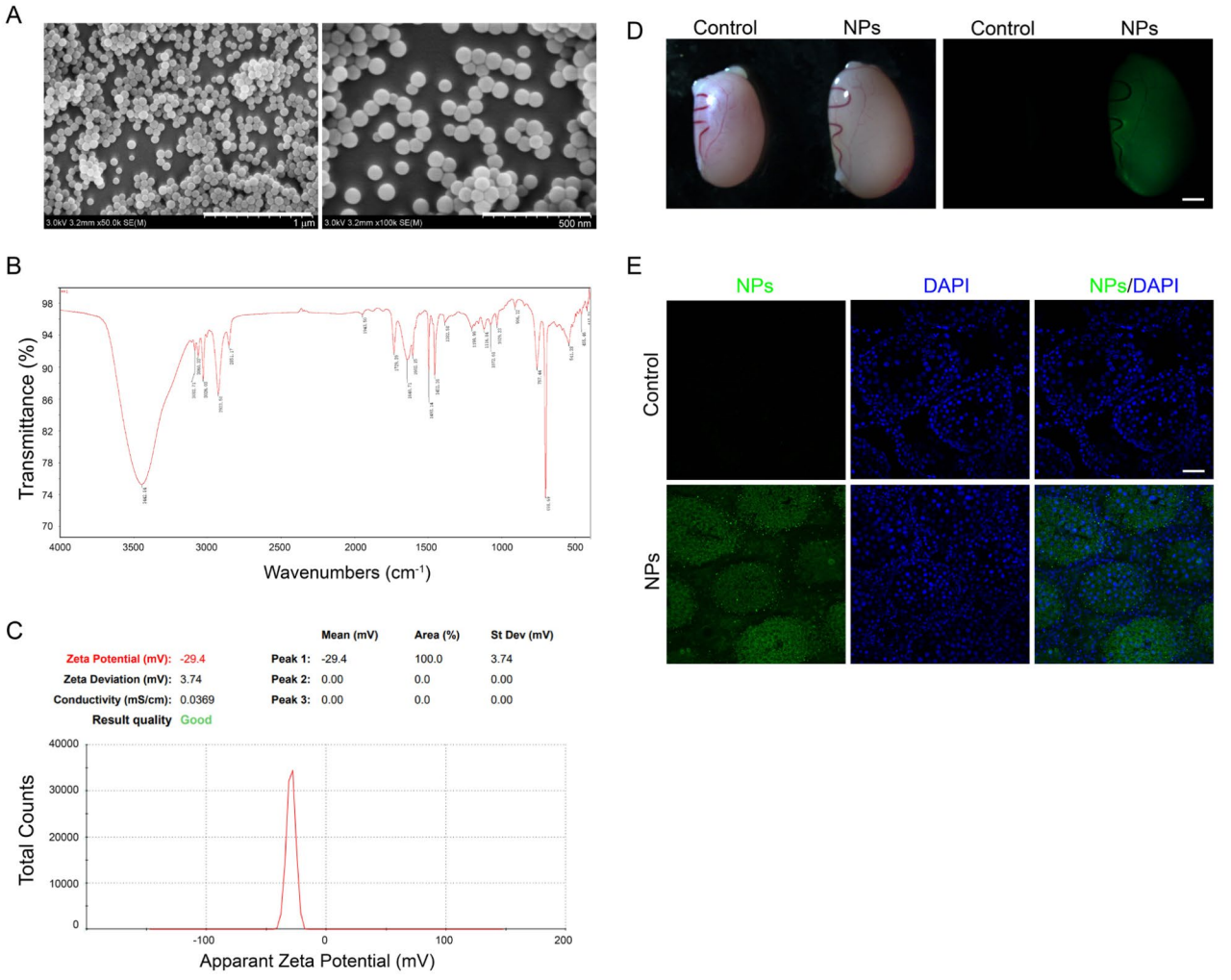

Fig. 1 Characteristics and testicular accumulation of PS-NPs. (**A**) Scanning electron microscope (SEM) micrographs display PS-NPs of 80 nm at different magnifications. Scale bar = 1 µm (left) or 500 nm (right). (**B**) Raman spectroscopic characterization of PS-NPs. (**C**) Zeta potential measurement of PS-NPs. (**D**) Fluorescent images of ex vivo rat testes detected by epifluorescence microscopy after one-week exposure to fluorescent PS-NPs (green) or ddH_2O (control). Scale bar = 2 mm. (**E**) Fluorescent images of rat testes cryosections detected by confocal microscopy after one-week exposure to fluorescent PS-NPs (green) or ddH_2O. Cell nuclei were stained with DAPI (blue). These images are representative findings of an experiment using $n = 5$ rats and yielded similar results. Scale bar = 10 µm.

PS-NPs in the testes, rats were orally administered with FITC-labeled PS-NPs. After a week of continuous gavage, animals were sacrificed and the ex vivo images of testis and cryosections were observed under fluorescent stereo and confocal microscope respectively, which revealed evident fluorescent signal distribution that represented PS-NPs accumulation in the testis (Fig. 1D) and seminiferous tubules (Fig. 1E) as compared with the non-treatment control group.

Pre-pubertal exposure to PS-NPs affects sperm quality and seminiferous tubule structure in rats after maturation

During the 10-week's oral gavage with PS-NPs from PND21, no significant difference on water consumption (Fig.S1A), food consumption (Fig.S1B), and body weight (Fig.S1C) was observed between control and NPs-treated groups over time. Further, changes in organ coefficients were evaluated at the end of treatment. Compared to the control group, the testicular coefficient significantly decreased in all the three NPs-treated groups (Fig.S1D), which may indicate a decreased testis function and affected spermatogenesis.

To evaluate sperm functions after PS-NPs exposure, the epididymal sperm smears on PND95 were prepared, which revealed increment of sperm anomalies in PS-NPs gavage groups, including loss of acrosome, headless, coiled tail, and tailless, etc., especially in the 6 and 12 mg/kg/day groups (Fig. 2A, B). Furthermore, sperm concentration and motility were found to decrease significantly in higher-dose groups (Fig. 2C, D). Then HE staining was

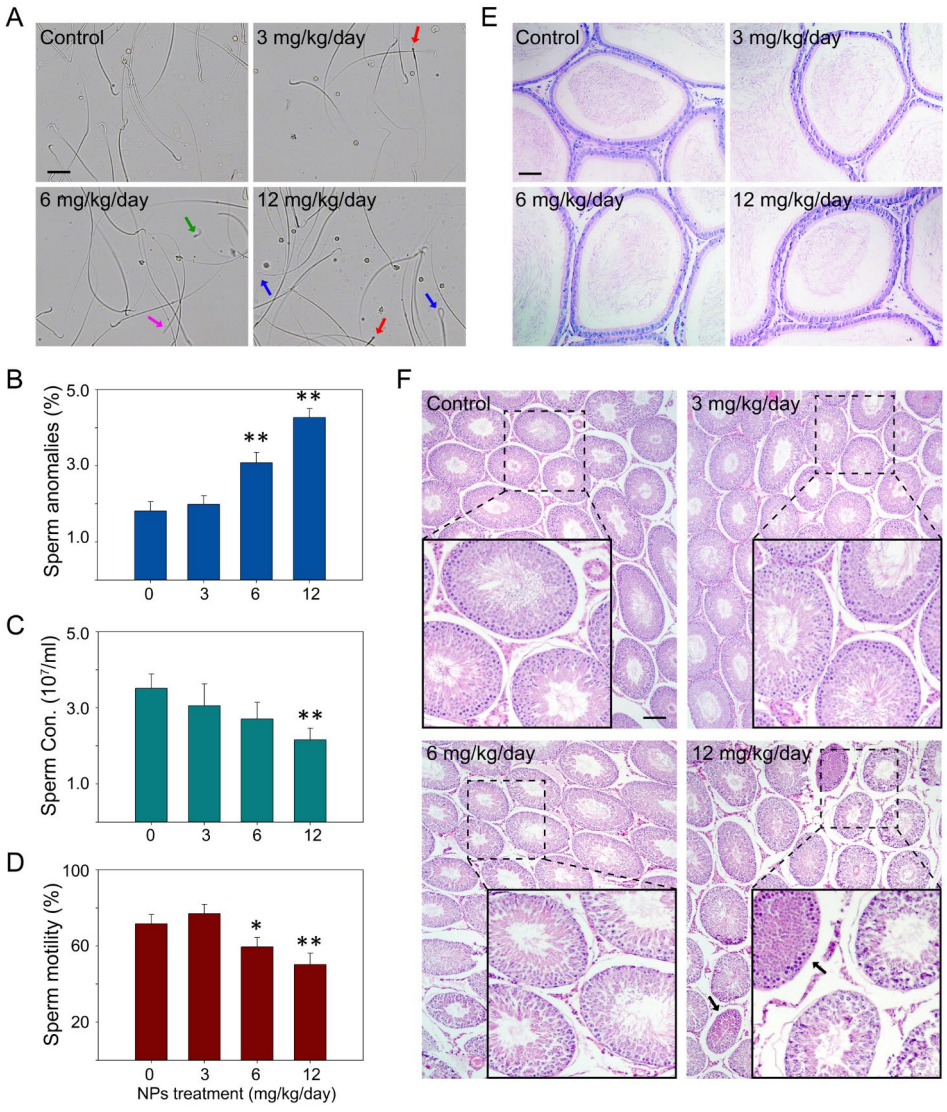

Fig. 2 Pre-pubertal exposure to PS-NPs affected sperm quality and seminiferous tubule structure in rats. (**A**) Epididymal sperm smear under light microscope on PND95. Main sperm abnormal morphologies: loss of acrosome (red arrow), headless (pink arrow), coiled tail (blue arrow), and tailless (green arrow). (B-D) Measurement of abnormal sperm rate (**B**), sperm concentration (**C**), and sperm vitality (**D**). Data is presented as mean ± SD ($n = 6$). *$P < 0.05$, **$P < 0.01$, compared with the control group. (E-F) H&E staining of cryosections of epididymis (**E**) and testis (**F**). The tubules pointed by the black arrows in the high-dose group were infiltrated with the round, deep-purple and nucleate neutrophile granulocytes. Dashed boxes are amplified to show clearer morphology. Scale bar = 60 μm (**E**) or 150 μm (**F**).

performed to detect the morphological change of epididymal ductus and seminiferous tubules. No obvious discrepancy was observed in the ductus structure between groups, while a reduction of epididymal sperm amount could be noticed as the dosage increased (Fig. 2E). The testicular injury of PS-NPs by gavage in our study was obvious yet not as serious as toxicants like cadmium. The images shown in Fig. 2F are representative of the overall situation. In the three treatment groups, a percentage of damaged tubules can be observed on each section, but not all the tubules are damaged. Rat testes exposed to PS-NPs exhibited increased percentage of damaged tubules (Fig.S2A), especially the 12 mg/kg/day group, characterized by contracted tubules, irregular and curved basement membranes, peeling of the spermatogenic cells from the epithelium, and inflammatory cell infiltration, indicating impaired spermatogenesis in response to PS-NPs gavage.

As continuous gavage of PS-NPs, serum of different groups was collected on PND55 and PND 95 and levels of reproductive hormones were estimated by ELISA. As shown in Fig. S2, on PND55 (i.e. after 5 weeks of continuous PS-NPs gavage), significant decrease in serum testosterone could be observed in the 6 and 12 mg/

kg/day groups whilst no variation in FSH and LH level amongst all groups. After 10 weeks of PS-NPs gavage (i.e. on PND95), both FSH and LH were reduced significantly in the 6 and 12 mg/kg/day groups while the level of testosterone declined in all the three treatment groups as compared with the control (Fig.S2B-D). These results indicated a negative correlation between PS-NPs exposure and reproductive hormone levels in a dose- and time-dependent manner.

Pre-pubertal exposure to PS-NPs induces BTB damage in a dose-dependent manner

Subsequently, we investigated the BTB integrity in animals gavaged with PS-NPs from pre-puberty. The permeability of BTB was measured by a semi-quantitative method using biotin as the tracer agent, with $CdCl_2$ treatment as the positive control and PBS as the negative control. After identifying the permeability of BTB in different groups, we found that, compared with the control in which the intact BTB intercepted the permeation of biotin into the lumen side, the distance of biotin infiltration from the basement of the tubule into the lumen progressively increased from the low to high dose groups, indicating a dose-dependent destructive effect of PS-NPs on BTB function (Fig. 3A, B).

Thereafter, the ultrastructure of BTB were detected under electron microscope (Fig. 3C). In the PS-NP-gavaged rat testis, especially the higher-dose treated groups, obvious cellular swelling within the seminiferous tubules could be observed, where cell membranes remained intact and continuous, while intracellular matrix electron density decreased as compared with the control; mitochondria (black arrows) were noticeably swollen, with some membrane damaged, extensive matrix dissolution, cristae rupture or disappearance, and severe vacuolization; the rough endoplasmic reticulum (red arrows) appeared slightly expanded, with ribosomes partially detached from its surface; lysosomal structures (dark yellow arrow) were visible in the field shown in 12 mg/kg/day group; the basement membrane (light yellow arrows) was continuous and uniform in thickness. Besides, local damage, blurring, and disappearance of BTB (green arrows in the treatment groups) occurred after PS-NPs treatment (Fig. 3C).

Due to the compromised BTB integrity after PS-NPs gavage from pre-puberty, we next examined the localization of junction proteins that constitute the barrier. The result of immunofluorescence showed that, after PS-NPs treatment for 10 weeks, the signal of occludin, ZO-1, and β-catenin were greatly weakened at the BTB (Fig. 4A-C).

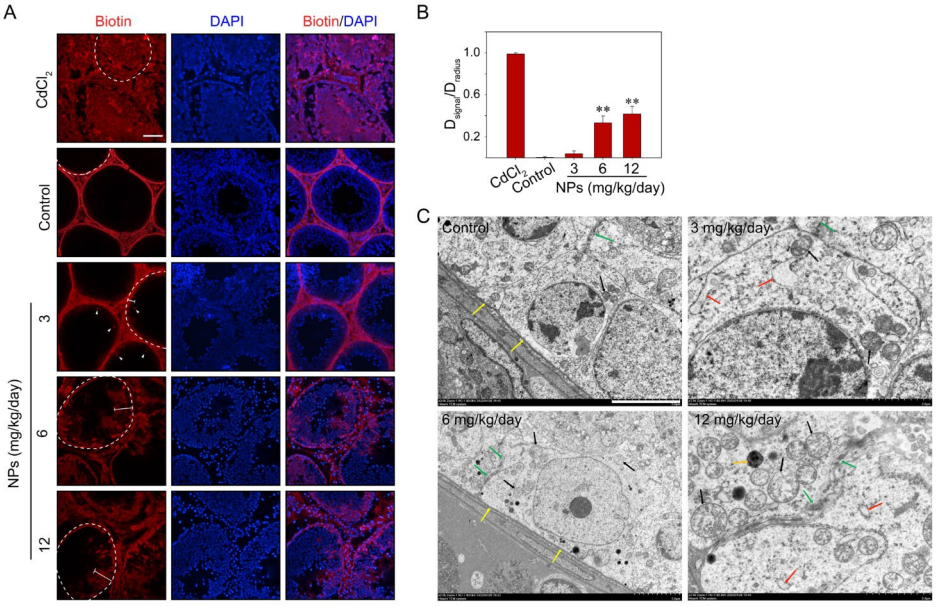

Fig. 3 PS-NPs disrupt BTB integrity in a dose-dependent manner. (**A**) In vivo BTB integrity assay by injecting EZ-Link Sulfo-NHS-LC-Biotin into the testis interstitium. The distribution of biotin was observed using specific Alexa Fluor 594-conjugated streptavidin (red), and cell nuclei were stained with DAPI (blue). Rats treated with $CdCl_2$ served as positive controls. White dashed lines denote the basement membrane of the seminiferous tubules, and white solid lines indicate the distance over which biotin diffused from the basement membrane to the tubular lumen, scale bar = 60 μm. (**B**) Semi-quantitative histogram illustrating the extent of biotin diffusion in each group of A. Each bar represents the average ratio of the biotin diffusion distance (D_{biotin}) to the tubular radius (D_{radius}) from 100 randomly selected seminiferous tubules from $n = 6$ parallel rats on PND95. $^{**}P < 0.01$, compared to the control group. (**C**) Ultrastructural changes in BTB induced by PS-NPs as observed under electron microscopy. Black arrow: mitochondria, red arrow: rough endoplasmic reticulum, dark yellow arrow: lysosome, light yellow arrow: basement membrane, green arrow: BTB. These images are representative findings of an experiment using $n = 6$ rats and yielded similar results. Scale bar = 1 μm.

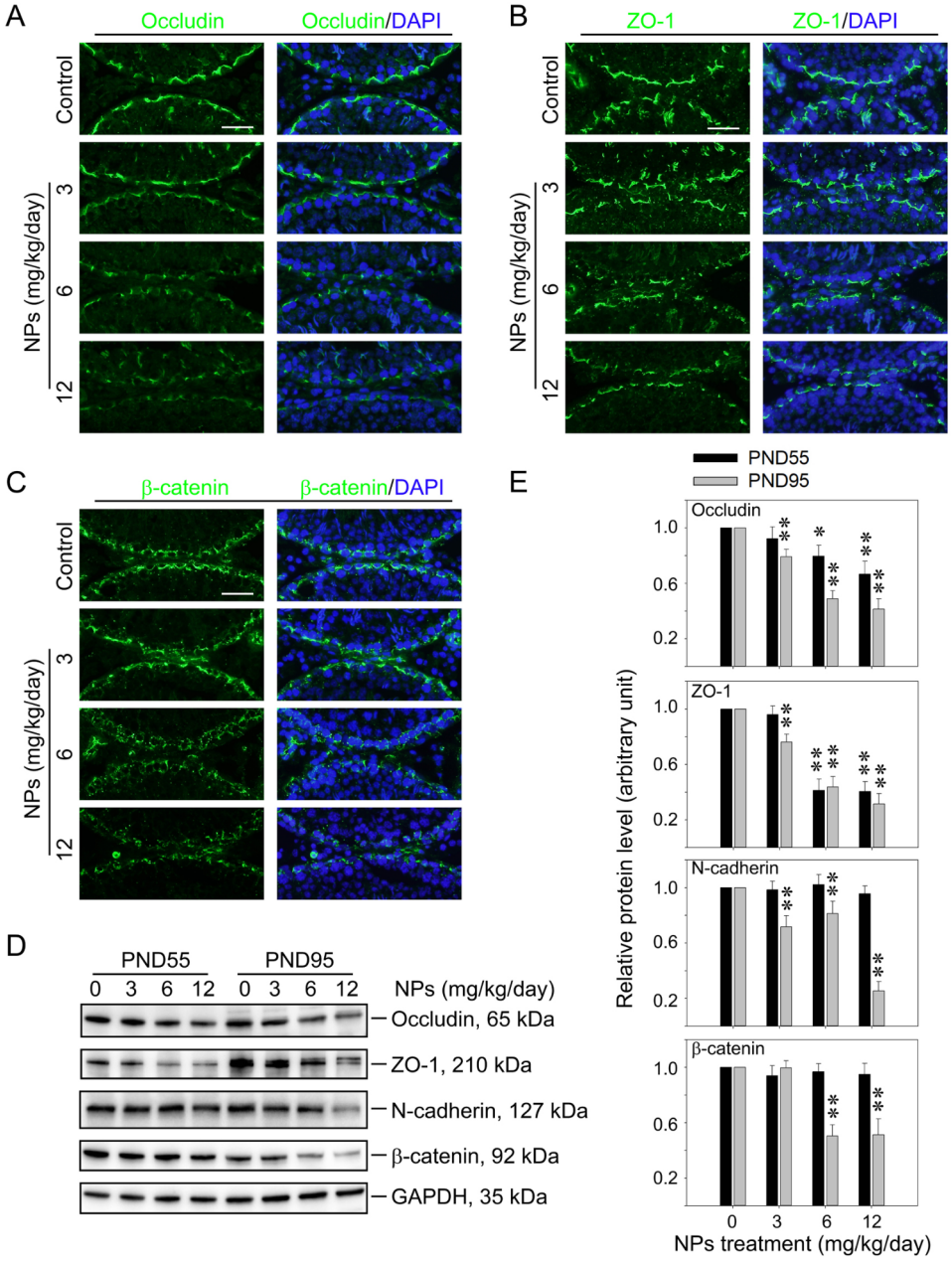

Fig. 4 Distribution and expression of junction proteins after PS-NPs treatment in rat testis. (A-C) Immunofluorescence analysis of occludin (**A**), ZO-1 (**B**), and β-catenin (**C**) on PND95. Secondary antibodies labeled with Alexa Fluor 488 (green) were used. Cell nuclei were stained with DAPI (blue), scale bar = 60 μm. (**D**) Western blot analysis to detect the levels of junction proteins on PND55 and PND95. (**E**) Box plots summarizing the result shown in D after each data point was normalized against GAPDH. Protein level of control group was arbitrarily set at 1. Data are represented as mean ± SD ($n = 6$). *$P < 0.05$ and **$P < 0.01$, compared with the control group.

Accordingly, Western blot also revealed significant reduction of occludin and ZO-1 in the testis of animals terminated on PND55 and PND95, while the level of N-cadherin and β-catenin decreased significantly only in samples on PND95 (Fig. 4D, E).

Pre-pubertal exposure to PS-NPs induces inflammatory response and apoptosis in rat testes

The immune homeostasis in the testis plays a critical role in spermatogenesis. In our study, the expression of interleukin-6 (IL-6), C-X-C motif chemokine ligand 10 (CXCL10), interleukin-1b (IL-1b), monocyte chemoattractant protein-1 (MCP-1), and tumor necrosis factor-α (TNF-α) in rat testis after PS-NPs treatment were detected by q-PCR on PND95. The results showed that

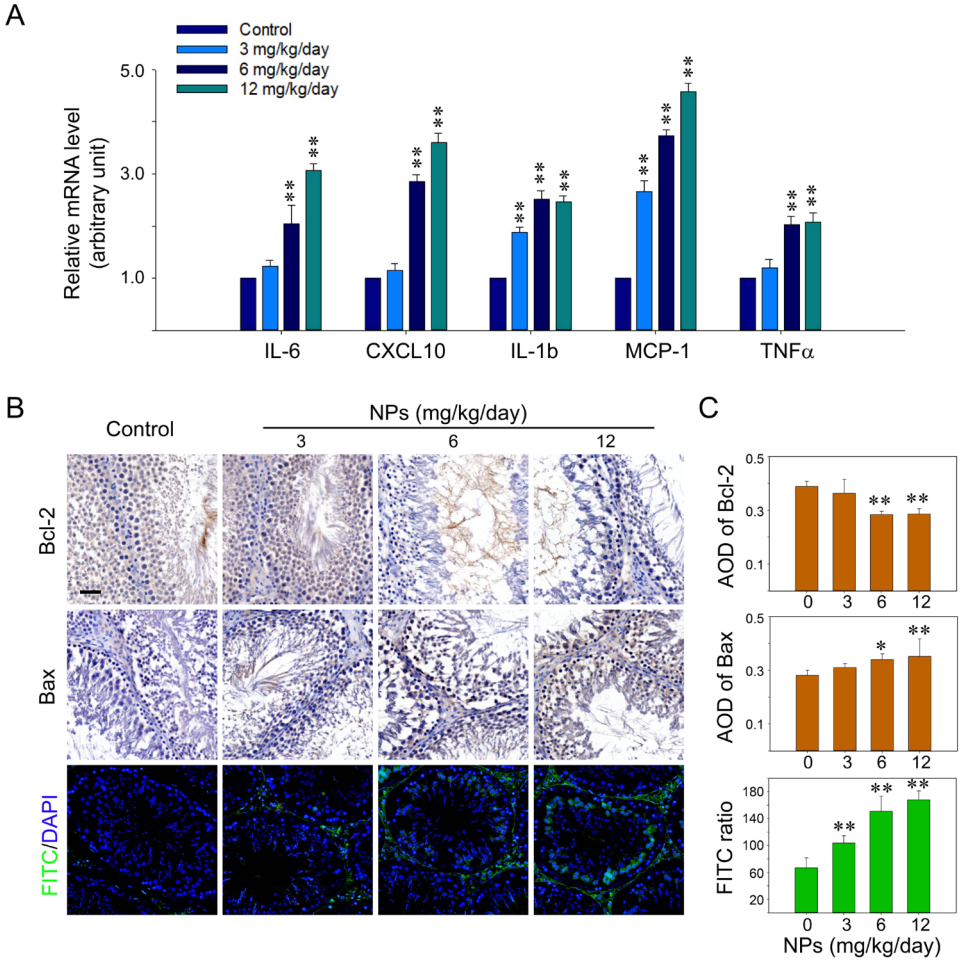

Fig. 5 Pre-pubertal exposure to PS-NPs induces inflammatory response and apoptosis in rat testes. (**A**) Histogram summarizing the result of quantitative real-time PCR in detecting relative mRNA levels of IL-6, CXCL10, IL-1b, MCP-1, and TNF-α in rat testes, which was expressed as a relative index normalized against GAPDH. Data are represented as mean ± SD ($n = 6$). (**B**) Immunohistochemistry staining of Bcl-2 (upper panel) and Bax (middle panel), and testicular TUNEL staining under LSCM (lower panel). Green fluorescence indicates TUNEL positive apoptotic cells. Scale bar = 50 μm. (**C**) Histograms summarizing the results in B to semi-quantify the average optical density (AOD) of Bcl-2 or Bax positive staining, and fluorescence intensity of TUNEL positive apoptotic cells by Image-Pro Plus software. Data are represented as mean ± SD. Each bar represents the average ratio of 12 microscopic fields randomly selected from $n = 6$ PND95 rats. $^{*}P < 0.05$, $^{**}P < 0.001$, compared to the control group.

the levels of these inflammatory factors in the testes of PS-NPs-treated rats significantly increased, indicating oral treatment of PS-NPs could lead to testicular inflammation (Fig. 5A). Then the indicators of apoptosis were detected by immunohistochemistry. Compared with the control, the expression of anti-apoptotic Bcl-2 decreased while the expression of pro-apoptotic Bax increased remarkably after PS-NPs treatment from pre-puberty (Fig. 5B, C). TUNEL staining also revealed significantly increased green granules representing apoptotic cells in response to PS-NPs treatment, signifying considerable apoptosis in testicular tissue (Fig. 5B, C).

TLR4 as the potential core target protein for PS-NPs action on rat testes

To elucidate the mechanisms of spermatogenic dysfunction caused by PS-NPs exposure, mRNA sequencing was conducted to screen differentially expressed genes (DEGs) between the control and PS-NPs exposed rat testis. Transcriptome profiling identified one hundred DEGs, including 53 up-regulated genes and 47 down-regulated genes (PS-NPs vs. control, Fig.S3A). GO enrichment analysis showed these DEGs mainly enriched in testicular tissue peptidase regulation, neutrophil activation, fatty acid transport, glucose transmembrane transport, monosaccharide transmembrane transport, production of nerve growth factor, snoRNA splicing, mesenchymal cell-matrix adhesion, and intermediate filament polymerization (Fig.S3B). KEGG enrichment analysis suggested that PS-NPs exposure primarily affects AMPK signaling, adipocytokine signaling, phosphatidylinositol signaling, lysosome, apoptosis, and autophagy in testis (Fig.S3C). In order to predict the principle target of polystyrene nanoparticles during testis damage, a PPI

network interaction diagram was created using styrene-interacting proteins and the above screened DEGs. As a result, toll-like receptor 4 (TLR4), the active transmembrane protein participating in inflammatory response, was identified as the core target that was responsible for testicular damage in rats caused by PS-NPs (Fig.S3D).

To further explore the interacting mechanism between TLR4 and PS-NPs, Schrödinger molecular docking software was applied to dock TLR4 with styrene monomer, trimer, and decamer, respectively (Fig. 6). The results showed that the docking score of TLR4 with styrene monomer was −4.466, indicating good binding. Specifically, styrene monomer interacts with the LYS817 of TLR4 via a π-π interaction and interacts with LEU819 via π-Alkyl interaction, suggesting these amino acid residues of TLR4 could be the binding sites of styrene monomer (Tab.S3). Two types of styrene polymers tested herein showed even better binding ability with TLR4 than monomer, with the docking score of -4.638 for the trimer and −5.784 for the decamer. The styrene trimer was revealed to interact with ARG729, ARG761, HIS726 of TLR4 via π-Alkyl interaction (Table S3). The styrene decamer shares some common binding sites with the trimer and could interact with GLU669 of TLR4 via π-Anion interaction, with GLY668 via π-Sigma interaction, and with ALA818 and ARG667 via π-Alkyl interaction (Tab.S3).

Cordycepin has strong competitive TLR4 binding ability with polystyrene

To further investigate potential drugs that can antagonize the binding of polystyrene with TLR4, we performed molecular docking of six known small antioxidant molecules, i.e. vitamin E (Vit E), coenzyme Q10 (CoQ10), docosahexaenoic acid (DHA), extract of ginkgo biloba (EGB), Salidroside, and Cordycepin, with TLR4 protein. Docking results were visualized using PyMOL and Discovery Studio 2019 (Fig. 7) and the specific residues of

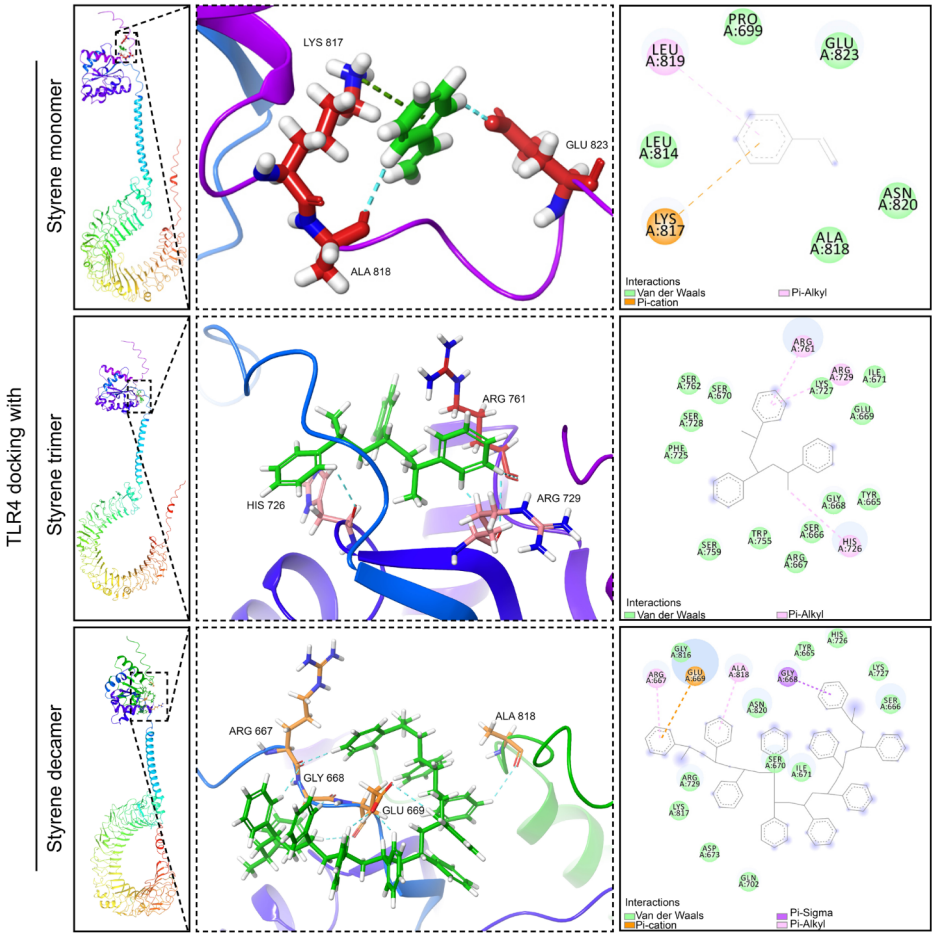

Fig. 6 TLR4 docking with different styrene molecules. Schrödinger molecular docking software analysis of the binding site of TLR4 with styrene monomer (upper), trimer (middle), and decamer (lower). The left images show the global docking between TLR4 and styrene molecules. Dashed boxes emphasize the local interaction and are amplified in the middle images. The right images are the 2D interaction of the docking. Different interactions between amino acid residues and styrene molecules are distinguished by different colors.

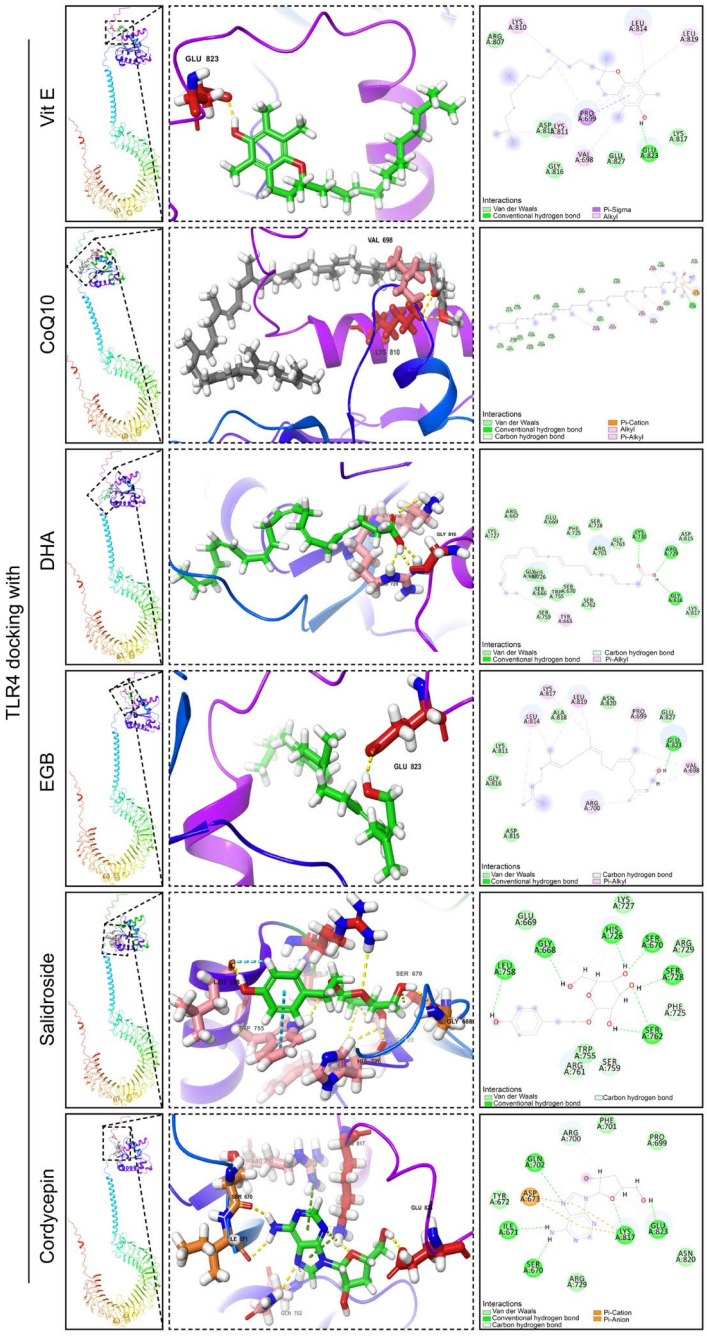

Fig. 7 TLR4 docking with small molecule antioxidant drugs. From top to bottom are respective docking of TLR4 with Vit E, CoQ10, DHA, EGB, Salidroside, and Cordycepin. The left images show the global dockings. The dashed areas are amplified in the middle to show local interaction of the dockings. The right images show the 2D interactions of the dockings.

TLR4 participating in different type of interaction with these drugs were summarized in Table S4. Generally, the greater the absolute value of the binding energy, the stronger the binding capacity. A binding energy below −5 kcal/mol indicates excellent interaction between the protein and compound. Our results show that Vit E, CoQ10, DHA, EGb, Salidroside, and Cordycepin can all bind to TLR4, with binding energy (kcal/mol) of -2.526, -4.422, -2.148, -2.204, -4.531, and −5.201, respectively (Tab.S4).

Among these interactions, some binding sites of Vit E, CoQ10, DHA, EGB, and Cordycepin with TLR4 were consistent with the binding sites of styrene monomer with TLR4, indicating that these five drugs had the

potential ability to compete with styrene to interact with TLR4. Similarly, CoQ10, DHA, Salidroside, and Cordycepin share certain interacting residues of TLR4 as the styrene trimer. And all the six drugs share certain interacting residues of TLR4 as the styrene decamer (Table S4). Summarily, among the six antioxidant compounds verified herein, Cordycepin can compete with various polymerized styrene molecules to bind with TLR4 protein and has the strongest binding ability.

Validation of binding affinity between Cordycepin and TLR4 through molecular dynamics simulation

Owing to the superior binding ability between Cordycepin and TLR4, we propose Cordycepin as a potential ideal therapeutic for polystyrene-induced reproductive damage in rats. To further validate the molecular docking results, a dynamic system of Cordycepin and TLR4 with water molecules as the solvent was successfully constructed, and the simulation system was neutralized by adding counter ions (Fig. 8A). The trajectory video of 100 ns demonstrated stable binding between Cordycepin and TLR4 without any trend of protein pocket dislocation (Fig. 8B). The Root Mean Square Deviation (RMSD) reflects the distance between identical atoms under different structural states. After a long-scale molecular dynamics simulation of 100 ns, the RMSD trend in the trajectory of the TLR4-Cordycepin system indicated relative stability, achieving a balanced state within 100 ns. The conformations and postures of the ligand were exceptionally stable (Fig. 8C).

The gyration radius (Rg) can indicate the tightness of protein structure, and also characterize the degree of peptide chain looseness during simulation. In the TLR4-Cordycepin system, the protein maintained excellent

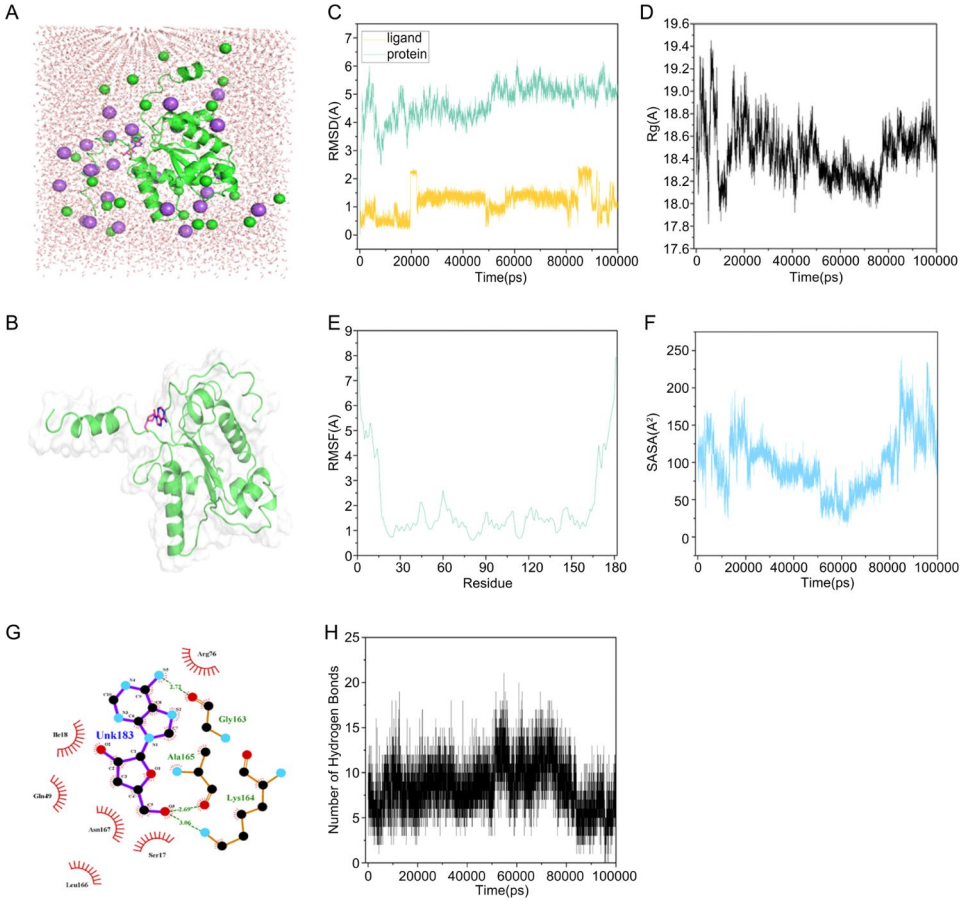

Fig. 8 Validation of binding affinity between Cordycepin and TLR4 through Molecular Dynamics Simulation. (**A**) A schematic diagram of the system construction. Sodium and chloride ions are counter ions and are added according to physiological concentrations. Purple ball: sodium ions, green ball: chloride ions, green cartoon: TLR4, purple stick: Cordycepin, red line: water molecules. (**B**) Final structure of Cordycepin-TLR4 complex. Green cartoon: TLR4, purple stick: Cordycepin, light grey: protein surface render. (**C**) RMSD reveals positional changes between protein conformation during simulation and initial conformation. Broken line in green, TLR4. Broken line in yellow, Cordycepin. (**D**) Rg characterizes the compactness of TLR4 structure in the TLR4-Cordycepin system. (**E**) RMSF reflects flexibility changes of TLR4 during simulation of TLR4-Cordycepin binding. (**F**) SASA measures the contribution of relative exposed surface area of Cordycepin in the TLR4 solvent over time. (**G**) Hydrogen bond analysis in the Cordycepin-TLR4 complex. Purple stick: Cordycepin, green dash line: hydrogen bond interactions, red eyelash: hydrophobic interactions. (**H**) Number of hydrogen bonds in the Cordycepin-TLR4 complex over time.

Table 1 Hydrogen bond interaction analysis of TLR4-Cordycepin*

Acceptor	DonorH	Donor	Frac	AvgDist	AvgAng
UNK_183@N2	ALA_165@H	ALA_165@N	0.6752	3.0897	158.6134
ASP_20@OD2	UNK_183@H10	UNK_183@O3	0.59	2.6442	164.9692
SER_17@O	UNK_183@H9	UNK_183@O2	0.5154	2.7401	162.4688
GLY_163@O	UNK_183@H13	UNK_183@N5	0.4941	2.9178	154.5367
ASP_20@CG	UNK_183@H10	UNK_183@O3	0.3912	3.3417	151.5031
UNK_183@N2	LYS_164@HA	LYS_164@CA	0.2876	3.4145	148.3526
ASP_20@OD1	UNK_183@H10	UNK_183@O3	0.2454	2.6853	163.8499
UNK_183@H8	LYS_164@HG3	LYS_164@CG	0.2309	3.293	152.9071

*3.5 Å was chosen as the cut-off distance

Table 2 Analysis of binding free energy (kcal/mol) between TLR4-Cordycepin using MM/PBSA

Energy Component	Average	Std. Dev.	Std. Err. of Mean
VDWAALS	-21.2329	4.6108	1.031
EEL	-31.0001	7.627	1.7055
EPB	41.8028	6.1974	1.3858
ENPOLAR	-2.4261	0.2456	0.0549
ΔG	-12.8564	4.5042	1.0072

VDWAALS: van der Waals energy, EEL: electrostatic energy, EPB: energy calculated by Poisson Boltzmann (PB) equation, ENPOLAR: nonpolar energy, ΔG: binding free energy

compactness throughout the simulation process, demonstrating overall stability (Fig. 8D). The Root Mean Square Fluctuation (RMSF) represents the average change in atomic position with time, indicating the degree of flexibility and movement of amino acids in protein throughout the simulation. Areas with greater flexibility have larger RMSF values. Overall, protein fluctuations in the TLR4-Cordycepin system were small, indicating stability. Large fluctuations occurred in the loop conformation around the C-terminal and N-terminal of the TLR4, consistent with the high flexibility and weak coupling features at the terminals (Fig. 8E). The Solvent Accessible Surface Area (SASA) characterizes changes in the surface area of the ligand directly accessible to the protein solvent over time, reflecting the relative contribution of the ligand surface area exposed to the solvent. In the TLR4-Cordycepin system, the SASA of Cordycepin fluctuated within a relatively constant scope, indicating it was tightly wrapped by the pocket of TLR4 (Fig. 8F), which is coincident with the stability observed in RMSD analysis.

Hydrogen bonds and hydrophobic interactions are crucial in maintaining protein conformation. The interaction between the binding pocket of protein and the ligand is important for the steady combination of the ligand. So we calculated the number of hydrogen bonds in the Cordycepin-TLR4 complex (Fig. 8G, H). For hydrogen bond analysis, 3.5 Å was chosen as the cut-off distance (Table 1). The system exhibits strong and stable hydrogen bond interactions, resulting in a steady dynamic conformation, which is consistent with the preceding analysis. Using the MM/PBSA method to calculate free energy, the binding free energy between TLR4 and Cordycepin was also revealed to be stable (Table 2).

Overall, the Cordycepin-TLR4 system displays excellent dynamic characteristics, validating the accuracy of docking posture. The ligand posture falls within a smaller conformational space domain, exhibiting stable dynamic characteristics. There exists strong binding energy and stable hydrogen bond interactions between the ligand and the protein.

Cordycepin inhibits PS-NPs induced oxidative stress and mitochondrial dysfunction in Sertoli cells

Next, the effect of Cordycepin on oxidative stress caused by PS-NPs was validated in primary rat Sertoli cells. Thirty minutes before PS-NPs (5, 20, or 100 μg/ml) treatment on culture day 3, Cordycepin (20 μg/ml) was administered to the SCs respectively. After 24 h, the cellular ROS level, CAT activity, and mitochondrial membrane potential were assessed by commercial kits. Consistent with the result in vivo, the primary SCs showed a high oxidative stress state induced by PS-NPs, reflected by significantly increased ROS signal and decreased CAT activity in a dose-dependent manner, which were greatly suppressed by Cordycepin (Fig. 9A, C and D). Mitochondrial membrane potential detection indicated that after Cordycepin treatment, the reduced red-green fluorescence ratio in SCs induced by PS-NPs was also markedly recovered (Fig. 9B and E), leading to elevation in mitochondrial membrane potential and restoration of normal function. These results suggest that Cordycepin can antagonize oxidative stress and mitochondrial dysfunction in Sertoli cells caused by PS-NPs, which might help with the impaired BTB function after PS-NPs intake.

Cordycepin alleviates PS-NPs induced BTB damage in primary Sertoli cells

In order to specify if the damage of PS-NPs on the BTB in vivo was due to its effect on SCs and to validate the effect of Cordycepin on BTB damaged by PS-NPs, the in vitro Sertoli cell epithelial barrier function was assessed after treatment of PS-NPs and Cordycepin. Daily measurement of TER found significantly declined barrier function triggered by 20 and 100 μg/ml PS-NPs, and no change was found in the 5 μg/ml group. Importantly, pre-treatment of Cordycepin (20 μg/ml) was shown to counteract the barrier function decline by more than 60%

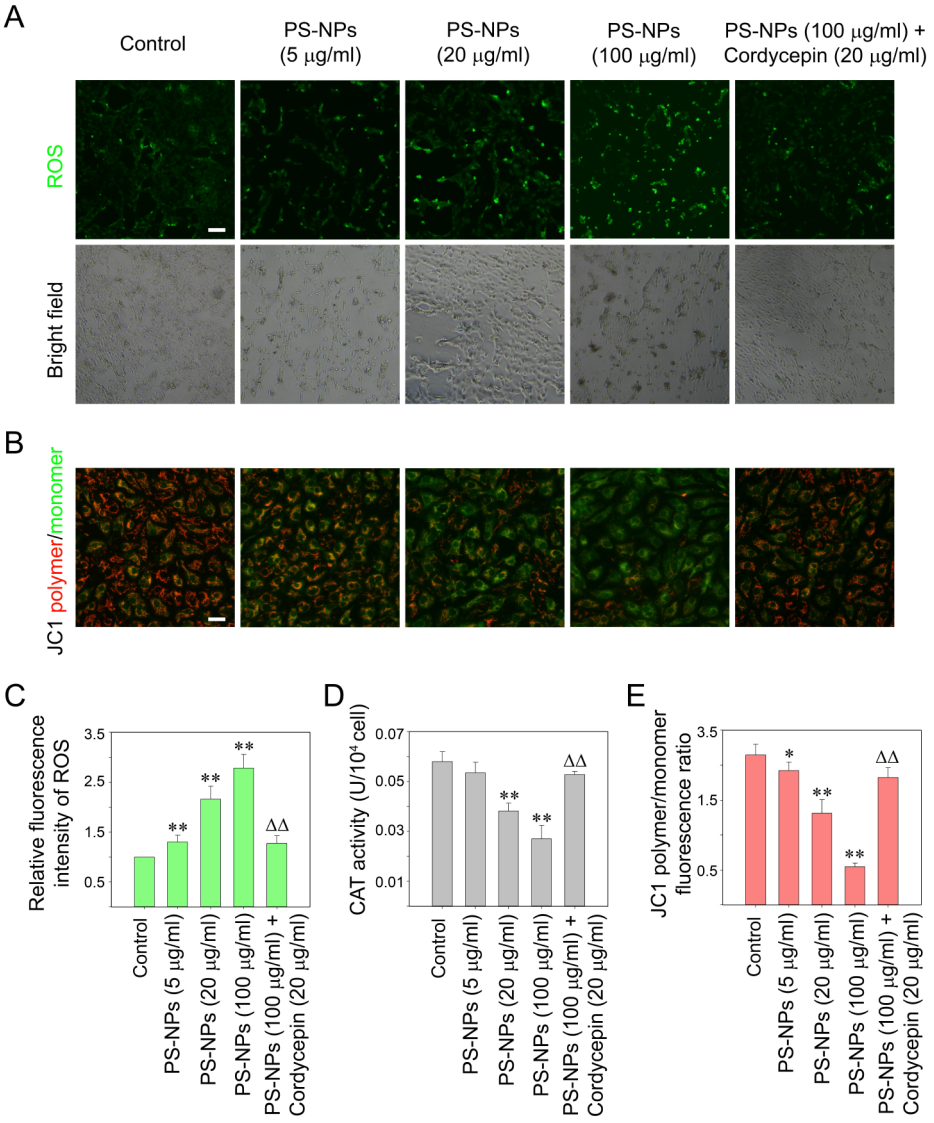

Fig. 9 Cordycepin inhibits oxidative stress and mitochondrial damage induced by PS-NPs in Sertoli cells. (**A**) Cellular reactive oxygen species detected by DCFH-DA (green). Pictures below are the same view field under light microscope. Scale bar = 150 μm. (**B**) JC-1 probe detecting mitochondrial membrane potential. Red fluorescence: probe aggregates. Green fluorescence: probe monomers. Scale bar = 40 μm. (**C**) A histogram illustrating the result in A after each data point was normalized to the control. (**D**) A histogram summarizing the CAT activity in Sertoli cells. (**E**) A histogram illustrating the result in B after calculating the red-green fluorescence ratio of the JC-1 probe. Data are represented as mean ± SD. Each bar represents the average ratio of 12 microscopic fields randomly selected from 3 different batches of primary cultured SCs. $^{**}P < 0.01$, compared to the control group. $^{\Delta}P < 0.05$, $^{\Delta\Delta}P < 0.01$, compared to the PS-NPs group.

in the 100 μg/ml PS-NPs group compared with the control (Fig. 10A). The Na-F permeability of the epithelium exhibited a similar trend, i.e. increased permeability after 20 and 100 μg/ml PS-NPs treatment that could be inhibited by Cordycepin (Fig. 10B). Immunofluorescence also revealed significantly diminished signals of BTB component proteins (occludin and β-catenin) at the SC-SC interface in PS-NPs group (Fig. 10C), which was also confirmed by immunoblot and could be partially rescued by Cordycepin treatment (Fig. 10D, E). These results further indicate the protection of Cordycepin on SC epithelial barrier impaired by PS-NPs.

Discussion

Plastic pollution is a global environmental problem that has made substantial negative impacts on several ecosystems. NPs is a recently recognized pollutant, which has been causing an increasing number of direct or indirect environmental issues due to their poor biodegradability and persistent accumulation. Previous studies have found that besides the digestive system, following treatment

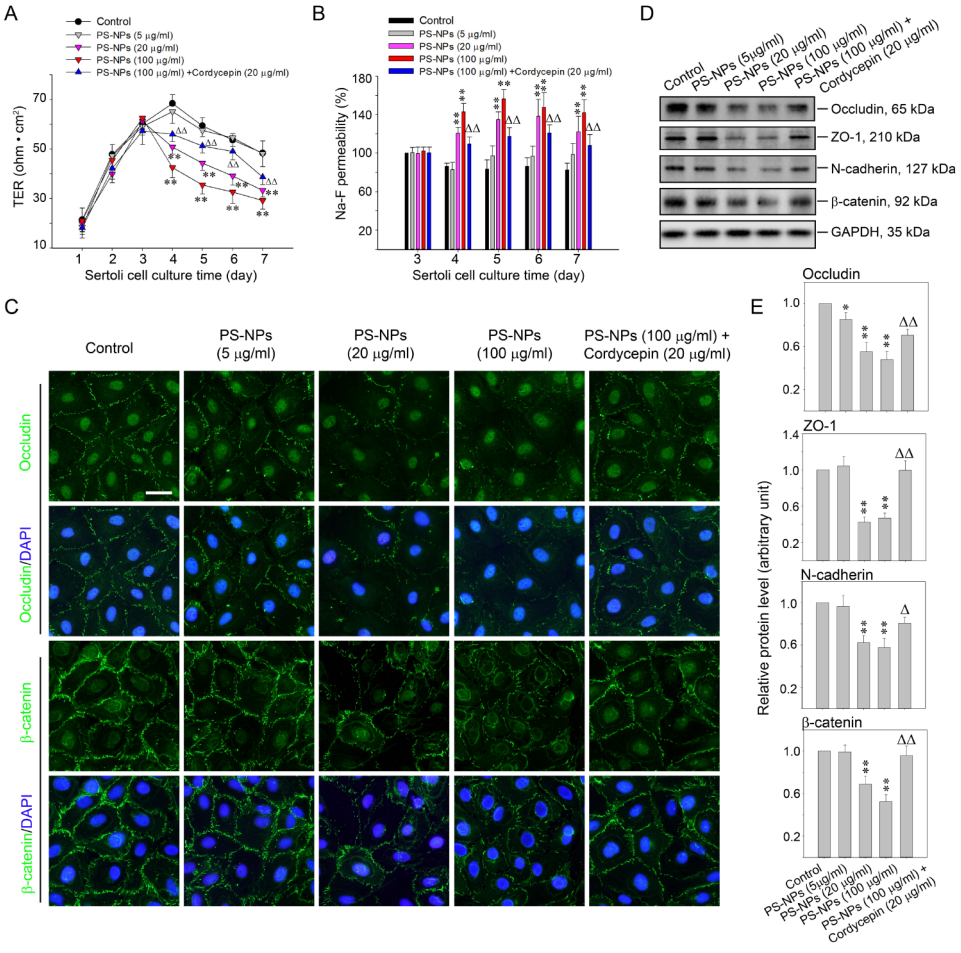

Fig. 10 Cordycepin counteracts the BTB damage caused by PS-NPs in rat Sertoli cells. (A and B) Barrier function analysis in vitro by recording TER (**A**) or measuring the permeability of Na-F (**B**) across the epithelium. The Na-F permeability in the control group on culture day 3 was arbitrarily set at 100%. $n=4$ parallel wells were set for each treatment group. The shown result is the representative of 3 independent experiments. (**C**) Immunofluorescence on culture day 5 using Alexa Fluor 488-conjugated secondary antibody (green) with cell nuclei stained with DAPI (blue) to observe occludin or β-catenin at cell-cell junctions. Scale bar = 40 μm. (**D**) Immunoblot analysis to assess the levels of different BTB proteins in SC lysates on culture day 5 after PS-NPs and Cordycepin treatment with GAPDH serving as a loading control. (**E**) Histograms summarizing the result shown in D after each data point was normalized against GAPDH. Protein level of the control group was arbitrarily set at 1. Each bar refers to mean ± SD of $n=3$ experiments using different batches of SC lysates. $^{*}P<0.05$, $^{**}P<0.01$, compared to the control group. $^{\Delta}P<0.05$, $^{\Delta\Delta}P<0.01$, compared to the PS-NPs group.

with fluorescently labeled NP particles, their signals were degressive in sequence of testis, brain, kidney, and lung [39], indicating that the testis is the primary accumulation and target organ of NPs. Since tissue accumulation of pollutants with lower environmental concentration may result in significant effects after a duration of contact, in this study we focused specifically on the accumulation of the NPs particles in the testis under our experimental conditions and observed obvious cumulation of the signal in the testis and seminiferous tubules, which was the basis for the rationality of the subsequent functional test results. To date, investigations on NPs in vitro mainly concentrated on macrophages and several epithelial cells [47–51]. Internal accumulation of PS-MPs has been proved to cause sperm abnormalities, arouse testicular inflammation, and damage the BTB in male mice [32, 52]. However, there is currently a lack of exploration into the toxic effects of PS-NPs on mammalian reproduction for assessing the human health risks associated with NPs.

The development of straightforward yet reliable analytical methods capable of detecting individual nanoparticles remains an ongoing challenge [53]. Some researchers also deemed that precautionary principle with the aim of recognizing critical dosages should be applied before evaluating the risk at environmental concentrations [36]. Therefore, lower dose of PS-NPs herein were selected to be 3 mg/kg/day to assess the environmentally relevant exposure dosages of nanoplastics according to the literature, and the relatively higher dosages (6 and 12 mg/kg/day) of PS-NPs were also investigated due to the large-scale production of plastics and bioaccumulation

of PS-NPs in the rat testis [36, 37]. Body weight, food-intake, water-intake, and the organ coefficient are frequently used indicators in toxicology, serving as sensitive indices for systemic toxicity [54]. In our model, the body weight, food- and water-intake did not show significant changes under the experimental dose design after ten weeks, excluding the possibility of changes caused by discrepant food- or water-intake. However, we observed a significant decrease in the rat's testicular coefficient post PS-NPs treatment, along with a marked reduction in the ratio of viable sperm in the epididymis. Since sperm is more sensitive to environmental factors than hormones [55], the evaluation of sperm characteristics can serve as useful indicators of male reproduction impairment. Our results show that with increasing concentrations of PS-NPs, the rate of sperm abnormalities in rats significantly increases, while the sperm count significantly decreases. This aligns with findings from reproductive hormone tests, i.e. the serum reproductive hormone concentration in the PS-NPs group was significantly downregulated, with testosterone levels drastically decreased in higher exposure groups. Testosterone, which promotes sperm maturation and release and maintains secondary sexual characteristics, is the most essential steroid hormone in the growth and development of male individuals. The decline in testosterone is a critical factor in reducing BTB integrity and testicular sperm [56]. Considering of this, future work should include the effect of PS-NPs on sterol metabolism of Leydig cells in the testis and the hypothalamus-pituitary-testicular axis. Even though, due to the direct influence of PS-NPs on SCs observed in vitro (Figs. 9 and 10), we consider the injured spermatogenesis as the combined result of hormone levels and the SC (or BTB) function. Hematoxylin-eosin staining results of testicular tissues also reveal contraction, irregular basement membrane, peeling of spermatogenic cells, and inflammatory cell infiltration in the seminiferous tubules, as well as lowered sperm density following PS-NPs treatment. PS-NPs exposure tends to damage rat seminiferous tubules, and the degree of testicular tissue cavitation and damage progressively exacerbates with increasing exposure concentrations. These observations suggest that PS-NPs may inflict some damage on rat sperm, resulting in decreased sperm quality. The testes are the most vital reproductive organs in males, and normal spermatogenic environment is necessary for maintaining sperm quality and normal reproductive capacity. Concurrently, these findings also affirm the feasibility of studying the damage of pre-pubertal exposure of PS-NPs on male rat reproduction through this model.

Bioavailable environmental pollutants can induce tissue inflammation. For instance, PS-MPs elevate the levels of IL-6 and TNFα in embryos of zebrafish [57]. A recent study in Balb/c mice also demonstrated that PS-MPs elevated the testicular tissue levels of TNFα, IL-6, and IL-1β [33]. MPs induce oxidative and inflammatory injury to germ cells in male zebrafish and oysters, thereby impacting offspring quantity and development [58]. In our experiments, a significant increase was observed in the expression of testicular tissue inflammatory factors as IL-6, CXCL10, IL-1b, MCP-1, and TNF-α, and pro-apoptotic factor Bax. TUNEL staining revealed an evident increase in testicular tissue cell apoptosis after PS-NPs treatment, reflecting the pro-apoptotic effect of PS-NPs after accumulation in the testis.

The BTB consists primarily of junction structures between SCs, generating a unique microenvironment for spermatogenesis [59–61]. At the BTB, cell adhesion relies on a variety of membrane proteins and their adaptors. For example, occludin and ZO-1 are major components of tight junctions. β-catenin interacts with calcium-dependent cell adhesion molecules such as N-cadherin, participating in the formation of the basement membrane adhesion complex. These junction proteins and their interactions contribute to establish solid intercellular connections by forming stable protein complexes, which are crucial for limiting abnormal traversal of substances at the BTB and protecting the stability of the spermatogenic environment [62]. After PS-NPs exposure in our study, electron microscopy showed changes of the BTB ultrastructure, while immunoblotting revealed a significant reduction of junction proteins (occludin, ZO-1, β-catenin, N-cadherin) in the testes. Immunofluorescence also indicated a reduced distribution of these proteins at the BTB, suggesting breakdown of junction apparatus at the BTB after exposure to PS-NPs. These results are consistent with the damage effect of PS-MPs on the BTB [29], and the consequent spermatogenic microenvironment damage might be one of the reasons for deteriorated sperm quality after exposure to PS-NPs in previous studies [25].

Toll-like receptors (TLRs), especially TLR4, are key modulators in inducing inflammation and activating mucosal immune responses [63], playing an indispensable role in environmental toxicant studies. Mice fed with MPs exhibit significant intestinal (colon and duodenum) inflammation, with increased levels of interferon regulatory factor 5 (IRF5), activator protein 1 (AP-1), and TLR4 [64]. Studies have shown that TLR4 can participate in oxidative stress caused by MPs, which can cause uterine fibrosis in mice by activating TLR4/NOX2 pathway and further provoking oxidative stress to stimuli Notch and TGF-β signaling [65]. Targeting the TLR4/NOX2 signaling pathway can effectively reduce the reproductive toxicity of PS-MPs [65]. In the present work, based on DEGs screened from transcriptome sequencing, the PPI network interaction diagram was made with styrene target proteins, and TLR4 was selected as the core

target protein for PS-NPs acting on rat testes. Through molecular docking, we further found that TLR4 can bind with both styrene monomer and polymers (trimer and decamer), suggesting PS-NPs particles might be incorporated into SCs through interaction with TLR4, thus inducing inflammation and oxidative stress.

Now a number of studies have shown small plastic particles can generate oxidative stress after internalization, then trigger corresponding biological effects. For example, PS-NPs of 50 nm in diameter have been found to be internalized and accumulate in HepG2 cells, induce oxidative stress, reduce antioxidative capacity, and lead to 25–48% cell death [49]. Uptake of PS-MPs by human renal proximal tubular epithelial cells (HK-2 cells) can lead to endoplasmic reticulum stress, dysfunction of mitochondria, and inflammation [66]. In brain, MPs-induced oxidative stress may have a bidirectional effect, i.e. DNA damage and mitochondrial dysfunction by attacking neurons, and ultimately result in cell death due to free radical attack [67]. In the reproductive field, sustained severe oxidative stress causes cell apoptosis or necrosis, and then continues to destroy BTB integrity, which has been proven as a crucial cause of male reproductive function impairment [68].

To find drugs that can effectively antagonize the reproductive impairment induced by PS-NPs in rats, we used molecular docking for simulation screening in this study. With the increase in structure numbers and resolution improvement within the Protein Data Bank (PDB), molecular docking has become a resource-saving early drug screening technology. As the damage caused by environmental pollutants is a long-term slow process, one focus of our therapeutic strategy exploration is to avoid long-term toxicity. For this purpose, we selected six commonly used non-toxic anti-oxidative stress drugs in the clinical practice of andrology in traditional Chinese and Western medicine. Vitamin E is an antioxidant, preventing degenerative diseases by scavenging reactive oxygen species [69, 70]. Standardized Extract of Ginkgo Biloba has been proved to regulate oxidative stress, energy deficiency, and spermatogenic status in rat testes induced by methotrexate [71]. Cordycepin is a primary bioactive component extracted from Cordyceps sinensis, with the efficacy of immune regulation, anti-cancer, anti-inflammatory, anti-oxidation, anti-bacterial, and is a potential drug for anti-aging and oxidative stress-induced male infertility [72]. Salidroside is an important active component separated from Cistanche salsa and possesses various pharmacological activities such as anti-oxidantion, anti-inflammatory, and anti-diabetis. Through molecular docking, we try to screen out small molecule drugs with binding sites consistent with the polystyrene target protein TLR4, which could compete with polystyrene for binding to TLR4. By comparing the binding ability of the six drugs, we found that Cordycepin has the best binding ability to TLR4, and the stability of Cordycepin-TLR4 complex was verified using molecular dynamics simulation. The antagonistic effects of Cordycepin on PS-NPs induced oxidative stress and BTB function impairment were further confirmed in a classical in vitro model that simulate the BTB using primary cultured rat Sertoli cells [73]. Therefore, Cordycepin could be a potentially ideal drug to block oxidative stress, protect spermatogenic microenvironment and prevent male reproductive damage caused by PS-NPs. Indeed, Cordycepin is probably not the only small antioxidant that can alleviate the BTB damage caused by PS-NPs, future studies should be focused on developing more effective therapeutics through small molecule drug screening technologies, for which our research is expected to provide valuable ideas.

Conclusion

In conclusion, this study shows that pre-puberty PS-NPs exposure disrupt the BTB integrity by inducing inflammatory responses and apoptosis in the rat testes which decrease the localization junction proteins at the BTB, thereby affecting the spermatogenic microenvironment and causing a decline in sperm count and motility after maturation. Our data indicates that PS-NPs exert toxic effects on rat testes by influencing a complex signal transduction network. Cordycepin can compete with polystyrene to bind its core target protein, TLR4, and relieving oxidative stress, making it a potential ideal drug for ameliorating male reproductive damage caused by PS-NPs. Although the polystyrene NPs used in this study cannot represent all the concentrations and types of nano plastics exist in the environment which fluctuate with different regions and policies on the planet, the inhibitory effect of Cordycepin on its reproductive toxicity is still worthy of further investigation. Future research is necessary to validate a more precise evaluation of the impacts of PS-NPs on male fertility in animals. Additionally, the study still need to be carried out to verify the protective effect of Cordycepin on reproductive toxicity caused by PS-NPs in vivo, determine the effective dose and side effects, and investigate its combined use with other drugs.

Supplementary Information

The online version contains supplementary material available at https://doi.org/10.1186/s12989-024-00590-w.

Supplementary Material 1

Supplementary Material 2

Supplementary Material 3

Supplementary Material 4

Supplementary Material 5

Supplementary Material 6

Supplementary Material 7

Author contributions
Y.H. performed most of the experiments and data analysis, and wrote most of the manuscript. S.J. performed part of data analysis. Q.Z. performed part of bioanalysis. W.Z. and J.L. performed part of immunoblotting and immunofluorescence. Y.X. wrote part of the manuscript. W.S. designed the experiments.

Funding
This work was supported by National Natural Science Foundation of China (81971442) to Wenhui Su, Natural Science Foundation of Liaoning Province (2023-MS-184) to Wenhui Su, Doctoral Scientific Research Foundation of Liaoning Province (2022-BS-145) to Ying Xu and Key Research and Development Plan Guidance Plan from Science and Technology Department of Liaoning Province (2018225081) to Wenhui Su.

Data availability
The data that support the findings of this study are available from the corresponding author upon reasonable request.

Declarations

Ethical approval
Animal feeding, caring, and experimental protocols were sanctioned by the Institutional Ethics Committee of China Medical University (Approval ID: CMU2021319).

Competing interests
The authors declare no competing interests.

Received: 23 March 2024 / Accepted: 25 July 2024
Published online: 09 August 2024

References

1. Young K, Song S, Hee H et al. Combined effects of UV exposure duration and mechanical abrasion on Microplastic Fragmentation by Polymer Type. 2017;51 8.
2. Xu B, Liu F, Brookes PC, Xu J. Microplastics play a minor role in tetracycline sorption in the presence of dissolved organic matter. Environmental pollution (Barking, Essex: 1987). 2018;240:87–94.
3. Jin Y, Xia J, Pan Z, Yang J, Wang W, Fu Z. Polystyrene microplastics induce microbiota dysbiosis and inflammation in the gut of adult zebrafish. Environ Pollution (Barking Essex: 1987). 2018;235(apr):322–9.
4. Wu J, Jiang R, Lin W, Ouyang G. Effect of salinity and humic acid on the aggregation and toxicity of polystyrene nanoplastics with different functional groups and charges. Environmental pollution (Barking, Essex: 1987). 2019;245:836 – 43.
5. Leslie HA, van Velzen MJM, Brandsma SH, Vethaak AD, Garcia-Vallejo JJ, Lamoree MH. Discovery and quantification of plastic particle pollution in human blood. Environ Int. 2022;163:107199. https://doi.org/10.1016/j.envint.2022.107199. https://www.ncbi.nlm.nih.gov/pubmed/35367073.
6. Li Z, Yi X, Zhou H, Chi T, Li W, Yang K. Combined effect of polystyrene microplastics and dibutyl phthalate on the microalgae Chlorella pyrenoidosa. Environ Pollut. 2020;257:113604. https://doi.org/10.1016/j.envpol.2019.113604. https://www.ncbi.nlm.nih.gov/pubmed/31761578.
7. Fournier SB, D'Errico JN, Adler DS, Kollontzi S, Goedken MJ, Fabris L, et al. Nanopolystyrene translocation and fetal deposition after acute lung exposure during late-stage pregnancy. Part Fibre Toxicol. 2020;17 1:55. https://doi.org/10.1186/s12989-020-00385-9. https://www.ncbi.nlm.nih.gov/pubmed/33099312.
8. Rist S, Carney Almroth B, Hartmann NB, Karlsson TM. A critical perspective on early communications concerning human health aspects of microplastics. Sci Total Environ. 2018;626:720–6. https://doi.org/10.1016/j.scitotenv.2018.01.092. https://www.ncbi.nlm.nih.gov/pubmed/29396337.
9. Schirinzi GF, Perez-Pomeda I, Sanchis J, Rossini C, Farre M, Barcelo D. Cytotoxic effects of commonly used nanomaterials and microplastics on cerebral and epithelial human cells. Environ Res. 2017;159:579 – 87; https://doi.org/10.1016/j.envres.2017.08.043. https://www.ncbi.nlm.nih.gov/pubmed/28898803
10. Zatorska-Plachta M, Lazarski G, Maziarz U, Forys A, Trzebicka B, Wnuk D, et al. Encapsulation of Curcumin in Polystyrene-based nanoparticles-drug loading capacity and cytotoxicity. ACS Omega. 2021;6 18:12168–78. https://doi.org/10.1021/acsomega.1c00867. https://www.ncbi.nlm.nih.gov/pubmed/34056370.
11. Wang L, Wu WM, Bolan NS, Dan T, Hou D. Environmental fate, toxicity and risk management strategies of nanoplastics in the environment: current status and future perspectives. J Hazard Mater. 2020;401:123415.
12. Rubio L, Barguilla I, Domenech J, Marcos R, Hernandez A. Biological effects, including oxidative stress and genotoxic damage, of polystyrene nanoparticles in different human hematopoietic cell lines - ScienceDirect. J Hazard Mater. 2020;398:122900.
13. Sun H, Jiao R, Wang D. The difference of aggregation mechanism between microplastics and nanoplastics: role of brownian motion and structural layer force. Essex: Environmental pollution (Barking; 1987. 2020;268 Pt B:115942.
14. Song YK, Hong SH, Eo S, Han GM, Shim WJ. Rapid Production of Micro- and nanoplastics by fragmentation of expanded polystyrene exposed to sunlight. Environ Sci Technol. 2020;54 18:11191–200.
15. Shi Q, Tang J, Wang L, Liu R, Giesy JP. Combined cytotoxicity of polystyrene nanoplastics and phthalate esters on human lung epithelial A549 cells and its mechanism. Ecotoxicol Environ Saf. 2021;213:112041. https://doi.org/10.1016/j.ecoenv.2021.112041. https://www.ncbi.nlm.nih.gov/pubmed/33601174.
16. Mruk DD, Su L, Cheng CY. Emerging role for drug transporters at the blood-testis barrier. Trends Pharmacol Sci. 2011;32 2:99–106. https://doi.org/10.1016/j.tips.2010.11.007.
17. Reis MM, Moreira AC, Sousa M, Mathur PP, Oliveira PF, Alves MG. Sertoli cell as a model in male reproductive toxicology: advantages and disadvantages. J Appl Toxicology: JAT. 2015;35 8:870–83. https://doi.org/10.1002/jat.3122.
18. Hu M, Palić D. Micro- and Nano-Plastics activation of oxidative and inflammatory adverse outcome pathways. Redox Biol. 2020;37:101620.
19. Jeong CB, Kang HM, Lee MC, Kim DH, Han J, Hwang DS, et al. Adverse effects of microplastics and oxidative stress-induced MAPK/Nrf2 pathway-mediated defense mechanisms in the marine copepod Paracyclopina Nana. Sci Rep. 2017;7:41323.
20. Wang J, Coffin S, Sun C, Schlenk D, Gan J. Negligible effects of microplastics on animal fitness and HOC bioaccumulation in earthworm Eisenia fetida in soil. Environ Pollution (Barking Essex: 1987). 2019;249:776–84.
21. Sussarellu R, Suquet M, Thomas Y, Lambert C, Fabioux C, Pernet ME, et al. Oyster reproduction is affected by exposure to polystyrene microplastics. Proc Natl Acad Sci U S A. 2016;113 9:2430–35.
22. Duan Z, Duan X, Zhao S, Wang X, Wang L. Barrier Function of Zebrafish Embryonic Chorions against Microplastics and nanoplastics and its impact on embryo development. J Hazard Mater. 2020;395 4:122621.
23. Marana MH, Poulsen R, Thormar EA, Clausen CG, Thit A, Mathiessen H, et al. Plastic nanoparticles cause mild inflammation, disrupt metabolic pathways, change the gut microbiota and affect reproduction in zebrafish: a full generation multi-omics study. J Hazard Mater. 2022;424 PtD:127705.
24. Pitt JA, Trevisan R, Massarsky A, Kozal JS, Levin ED, Di Giulio RT. Maternal transfer of nanoplastics to offspring in zebrafish (Danio rerio): a case study with nanopolystyrene. Sci Total Environ. 2018;643:324–34.
25. Xu W, Yuan Y, Tian Y, Cheng C, Chen Y, Zeng L, et al. Oral exposure to polystyrene nanoplastics reduced male fertility and even caused male infertility by inducing testicular and sperm toxicities in mice. J Hazard Mater. 2023;454:131470. https://doi.org/10.1016/j.jhazmat.2023.131470. https://www.ncbi.nlm.nih.gov/pubmed/37116333.
26. Mruk DD, Cheng CY. The mammalian blood-testis barrier: its Biology and Regulation. Endocr Rev. 2015;36 5:564–91. https://doi.org/10.1210/er.2014-1101. https://www.ncbi.nlm.nih.gov/pubmed/26357922.
27. Jia X, Xu Y, Wu W, Fan Y, Wang G, Zhang T, et al. Aroclor1254 disrupts the blood-testis barrier by promoting endocytosis and degradation of junction proteins via p38 MAPK pathway. Cell Death Dis. 2017;8 5:e2823. https://doi.org/10.1038/cddis.2017.224. https://www.ncbi.nlm.nih.gov/pubmed/28542131.
28. Wan HT, Mruk DD, Wong CK, Cheng CY. Targeting testis-specific proteins to inhibit spermatogenesis: lesson from endocrine disrupting chemicals. Expert

Opin Ther Targets. 2013;17 7:839–55. https://doi.org/10.1517/14728222.2013.791679. https://www.ncbi.nlm.nih.gov/pubmed/23600530.
29. Li S, Wang Q, Yu H, Yang L, Sun Y, Xu N, et al. Polystyrene microplastics induce blood-testis barrier disruption regulated by the MAPK-Nrf2 signaling pathway in rats. Environ Sci Pollut Res Int. 2021;28 35:47921–31. https://doi.org/10.1007/s11356-021-13911-9. https://www.ncbi.nlm.nih.gov/pubmed/33895957.
30. Wei Y, Zhou Y, Long C, Wu H, Hong Y, Fu Y, et al. Polystyrene microplastics disrupt the blood-testis barrier integrity through ROS-Mediated imbalance of mTORC1 and mTORC2. Environ Pollut. 2021;289:117904. https://doi.org/10.1016/j.envpol.2021.117904. https://www.ncbi.nlm.nih.gov/pubmed/34371264.
31. Ijaz MU, Shahzadi S, Samad A, Ehsan N, Ahmed H, Tahir A, et al. Dose-dependent effect of Polystyrene Microplastics on the testicular tissues of the male Sprague Dawley rats. Dose Response. 2021;19 2:15593258211019882. https://doi.org/10.1177/15593258211019882. https://www.ncbi.nlm.nih.gov/pubmed/34158809.
32. Jin H, Ma T, Sha X, Liu Z, Zhou Y, Meng X, et al. Polystyrene microplastics induced male reproductive toxicity in mice. J Hazard Mater. 2021;401:123430. https://doi.org/10.1016/j.jhazmat.2020.123430. https://www.ncbi.nlm.nih.gov/pubmed/32659591.
33. Xie X, Deng T, Duan J, Xie J, Yuan J, Chen M. Exposure to polystyrene microplastics causes reproductive toxicity through oxidative stress and activation of the p38 MAPK signaling pathway. Ecotoxicol Environ Saf. 2020;190:110133. https://doi.org/10.1016/j.ecoenv.2019.110133. https://www.ncbi.nlm.nih.gov/pubmed/31896473.
34. Zhang J, Wang L, Trasande L, Kannan K. Occurrence of polyethylene terephthalate and polycarbonate microplastics in infant and adult feces. Environ Sci Technol Lett. 2021;8 11:989–94. https://doi.org/10.1021/acs.estlett.1c00559.
35. Zhou Y, Zhong X, Chen L, Gong L, Luo L, He Q, et al. Gut microbiota combined with metabolome dissects long-term nanoplastics exposure-induced disturbed spermatogenesis. Ecotoxicol Environ Saf. 2023;267:115626. https://doi.org/10.1016/j.ecoenv.2023.115626. https://www.ncbi.nlm.nih.gov/pubmed/37890247.
36. Rafiee M, Dargahi L, Eslami A, Beirami E, Jahangiri-Rad M, Sabour S, et al. Neurobehavioral assessment of rats exposed to pristine polystyrene nanoplastics upon oral exposure. Chemosphere. 2018;193:745–53. https://doi.org/10.1016/j.chemosphere.2017.11.076. https://www.ncbi.nlm.nih.gov/pubmed/29175402.
37. Amereh F, Eslami A, Fazelipour S, Rafiee M, Zibaii MI, Babaei M. Thyroid endocrine status and biochemical stress responses in adult male Wistar rats chronically exposed to pristine polystyrene nanoplastics. Toxicol Res (Camb). 2019. https://doi.org/10.1039/c9tx00147f. 8 6:953 – 63; doi:. https://www.ncbi.nlm.nih.gov/pubmed/34055310.
38. Jiang S, Xu Y, Fan Y, Hu Y, Zhang Q, Su W. Busulfan impairs blood-testis barrier and spermatogenesis by increasing noncollagenous 1 domain peptide via matrix metalloproteinase 9. Andrology. 2022;10 2:377–91. https://doi.org/10.1111/andr.13112. https://www.ncbi.nlm.nih.gov/pubmed/34535976.
39. Xu D, Ma Y, Han X, Chen Y. Systematic toxicity evaluation of polystyrene nanoplastics on mice and molecular mechanism investigation about their internalization into Caco-2 cells. J Hazard Mater. 2021;417:126092. https://doi.org/10.1016/j.jhazmat.2021.126092. https://www.ncbi.nlm.nih.gov/pubmed/34015712.
40. Zhang X, Zhang Q, Huang L, Liu M, Cheng Z, Zheng Y, et al. Pien-Tze-Huang attenuates neuroinflammation in cerebral ischaemia-reperfusion injury in rats through the TLR4/NF-kappaB/MAPK pathway. Pharm Biol. 2021;59 1:828–39. https://doi.org/10.1080/13880209.2021.1942926. https://www.ncbi.nlm.nih.gov/pubmed/34196587.
41. Zhang K, Wu L, Lin K, Zhang M, Li W, Tong X, et al. Integrin-dependent microgliosis mediates ketamine-induced neuronal apoptosis during postnatal rat retinal development. Exp Neurol. 2021;340:113659. https://doi.org/10.1016/j.expneurol.2021.113659. https://www.ncbi.nlm.nih.gov/pubmed/33640375.
42. Case DA, Duke RE, Walker RC, Skrynnikov NR, Cheatham TE III, Mikhailovskii O et al. AMBER 22 Reference Manual. 2022.
43. Tian C, Kasavajhala K, Belfon KAA, Raguette L, Huang H, Migues AN, et al. ff19SB: amino-acid-specific protein backbone parameters trained against Quantum Mechanics Energy Surfaces in Solution. J Chem Theory Comput. 2020;16(1):528–52. https://doi.org/10.1021/acs.jctc.9b00591.
44. Wu W, Hu Y, Zhang Q, Xu Y, Su W. TNFalpha stimulates the proliferation of immature Sertoli cells by attenuating UPS-degradation of cyclin D1 and leads to the delay of BTB maturation in pubertal rats. Andrology. 2023;11 3:575–90. https://doi.org/10.1111/andr.13336. https://www.ncbi.nlm.nih.gov/pubmed/36354278.
45. Xu Y, Jiang S, Hu Y, Zhang Q, Su W. TGF-beta3 induces lactate production in Sertoli cell through inhibiting the notch pathway. Andrology. 2022;10 8:1644–59. https://doi.org/10.1111/andr.13288. https://www.ncbi.nlm.nih.gov/pubmed/36057850.
46. Xu Y, Wu W, Fan Y, Jiang S, Jia X, Su W. MiR-142-3p inhibits TGF-beta3-Induced blood-testis barrier impairment by targeting Lethal Giant Larvae Homolog 2. Cell Physiol Biochem. 2018;46 1:253–68. https://doi.org/10.1159/000488427. https://www.ncbi.nlm.nih.gov/pubmed/29590647.
47. Kuhn DA, Vanhecke D, Michen B, Blank F, Gehr P, Petri-Fink A, et al. Different endocytotic uptake mechanisms for nanoparticles in epithelial cells and macrophages. Beilstein J Nanotechnol. 2014;5:1625–36. https://doi.org/10.3762/bjnano.5.174.
48. Busch M, Bredeck G, Kämpfer AAM, Schins RPF. Investigations of acute effects of polystyrene and polyvinyl chloride micro- and nanoplastics in an advanced in vitro triple culture model of the healthy and inflamed intestine. Environ Res. 2021;193:110536. https://doi.org/10.1016/j.envres.2020.110536.
49. He Y, Li J, Chen J, Miao X, Li G, He Q, et al. Cytotoxic effects of polystyrene nanoplastics with different surface functionalization on human HepG2 cells. Sci Total Environ. 2020;723:138180. https://doi.org/10.1016/j.scitotenv.2020.138180.
50. Xu M, Halimu G, Zhang Q, Song Y, Fu X, Li Y, et al. Internalization and toxicity: a preliminary study of effects of nanoplastic particles on human lung epithelial cell. Sci Total Environ. 2019;694:133794. https://doi.org/10.1016/j.scitotenv.2019.133794.
51. Ding Y, Zhang R, Li B, Du Y, Li J, Tong X, et al. Tissue distribution of polystyrene nanoplastics in mice and their entry, transport, and cytotoxicity to GES-1 cells. Environ Pollution (Barking Essex: 1987). 2021;280:116974. https://doi.org/10.1016/j.envpol.2021.116974.
52. Hou B, Wang F, Liu T, Wang Z. Reproductive toxicity of polystyrene microplastics: in vivo experimental study on testicular toxicity in mice. J Hazard Mater. 2021;405:124028. https://doi.org/10.1016/j.jhazmat.2020.124028.
53. Xu G, Cheng H, Jones R, Feng Y, Gong K, Li K, et al. Surface-enhanced Raman Spectroscopy Facilitates the Detection of Microplastics < 1 mum in the Environment. Environ Sci Technol. 2020;54 24:15594–603. https://doi.org/10.1021/acs.est.0c02317. https://www.ncbi.nlm.nih.gov/pubmed/33095569.
54. Piao Y, Liu Y, Xie X. Change trends of organ weight background data in Sprague Dawley rats at different ages. J Toxicologic Pathol. 2013;26 1:29–34. https://doi.org/10.1293/tox.26.29.
55. Garcia T, Schreiber E, Kumar V, Prasad R, Sirvent JJ, Domingo JL et al. Effects on the reproductive system of young male rats of subcutaneous exposure to n-butylparaben. Food and chemical toxicology: an international journal published for the British Industrial Biological Research Association. 2017;106 Pt A:47–57; https://doi.org/10.1016/j.fct.2017.05.031
56. Siu ER, Wong EW, Mruk DD, Porto CS, Cheng CY. Focal adhesion kinase is a blood-testis barrier regulator. Proc Natl Acad Sci U S A. 2009;106 23:9298–303. https://doi.org/10.1073/pnas.0813113106.
57. Zhang X, Shi J, Yuan P, Li T, Cao Z, Zou W. Differential developmental and proinflammatory responses of zebrafish embryo to repetitive exposure of biodigested polyamide and polystyrene microplastics. J Hazard Mater. 2023;460:132472. https://doi.org/10.1016/j.jhazmat.2023.132472. https://www.ncbi.nlm.nih.gov/pubmed/37683353.
58. Lee WS, Cho HJ, Kim E, Huh YH, Kim HJ, Kim B, et al. Bioaccumulation of polystyrene nanoplastics and their effect on the toxicity of au ions in zebrafish embryos. Nanoscale. 2019;11 7:3173–85. https://doi.org/10.1039/c8nr09321k.
59. Lu Y, Luo B, Li J, Dai J. Perfluorooctanoic acid disrupts the blood-testis barrier and activates the TNFalpha/p38 MAPK signaling pathway in vivo and in vitro. Arch Toxicol. 2016;90(4):971–83. https://doi.org/10.1007/s00204-015-1492-y. http://www.ncbi.nlm.nih.gov/pubmed/25743374.
60. Yan HH, Mruk DD, Lee WM, Cheng CY. Blood-testis barrier dynamics are regulated by testosterone and cytokines via their differential effects on the kinetics of protein endocytosis and recycling in Sertoli cells. FASEB journal: official publication of the Federation of American Societies for Experimental Biology. 2008;22 6:1945–59; https://doi.org/10.1096/fj.06-070342. http://www.ncbi.nlm.nih.gov/pubmed/18192323
61. Cheng CY, Mruk DD. The blood-testis barrier and its implications for male contraception. Pharmacol Rev. 2012;64(1):16–64. https://doi.org/10.1124/pr.110.002790. ://WOS:000298409100002.

62. Cheng CY, Mruk DD. The blood-testis barrier and its implications for male contraception. Pharmacol Rev. 2012;64 1:16–64. https://doi.org/10.1124/pr.110.002790. https://www.ncbi.nlm.nih.gov/pubmed/22039149.
63. Szebeni B, Veres G, Dezsõfi A, Rusai K, Vannay A, Mraz M, et al. Increased expression of toll-like receptor (TLR) 2 and TLR4 in the colonic mucosa of children with inflammatory bowel disease. Clin Exp Immunol. 2008;151(1):34–41. https://doi.org/10.1111/j.1365-2249.2007.03531.x.
64. Li B, Ding Y, Cheng X, Sheng D, Xu Z, Rong Q, et al. Polyethylene microplastics affect the distribution of gut microbiota and inflammation development in mice. Chemosphere. 2020;244:125492. https://doi.org/10.1016/j.chemosphere.2019.125492.
65. Wu H, Xu T, Chen T, Liu J, Xu S. Oxidative stress mediated by the TLR4/NOX2 signalling axis is involved in polystyrene microplastic-induced uterine fibrosis in mice. Sci Total Environ. 2022;838:155825. https://doi.org/10.1016/j.scitotenv.2022.155825. https://www.ncbi.nlm.nih.gov/pubmed/35597360.
66. Wang YL, Lee YH, Hsu YH, Chiu IJ, Huang CC, Huang CC et al. The kidney-related effects of Polystyrene Microplastics on human kidney proximal tubular epithelial cells HK-2 and male C57BL/6 mice. Environmental health perspectives. 2021;129 5:57003; https://doi.org/10.1289/ehp7612
67. Kahroba H, Ramezani B, Maadi H, Sadeghi MR, Jaberie H, Ramezani F. The role of Nrf2 in neural stem/progenitors cells: from maintaining stemness and self-renewal to promoting differentiation capability and facilitating therapeutic application in neurodegenerative disease. Ageing Res Rev. 2021;65:101211. https://doi.org/10.1016/j.arr.2020.101211.
68. Møller P, Danielsen PH, Karottki DG, Jantzen K, Roursgaard M, Klingberg H, et al. Oxidative stress and inflammation generated DNA damage by exposure to air pollution particles. Mutat Res Reviews Mutat Res. 2014;762:133–66. https://doi.org/10.1016/j.mrrev.2014.09.001.
69. Meydani M, Vitamin E, Lancet, London. England). 1995;345 8943:170–5. https://doi.org/10.1016/s0140-6736(95)90172-8.
70. Niki E, Traber MG. A history of vitamin E. Ann Nutr Metab. 2012;61(3):207–12. https://doi.org/10.1159/000343106.
71. Mansour DF, Saleh DO, Ahmed-Farid OA, Rady M, Bakeer RM, Hashad IM. Ginkgo biloba extract (EGb 761) mitigates methotrexate-induced testicular insult in rats: targeting oxidative stress, energy deficit and spermatogenesis. Biomed Pharmacotherapy = Biomedecine Pharmacotherapie. 2021;143:112201. https://doi.org/10.1016/j.biopha.2021.112201.
72. Kopalli SR, Cha KM, Cho JY, Kim SK, Koppula S. Cordycepin mitigates spermatogenic and redox related expression in H2O2-exposed leydig cells and regulates testicular oxidative apoptotic signalling in aged rats. Pharm Biol. 2022;60(1):404–16.
73. Mruk DD, Cheng CY. An in vitro system to study Sertoli cell blood-testis barrier dynamics. Methods Mol Biol. 2011;763:237–52. https://www.ncbi.nlm.nih.gov/pubmed/21874456. doi: 10.1007/978-1-61779-191-8_16.

Publisher's Note